Cell

Reconstruction of a fatty acid synthesis cycle from acyl carrier protein and cofactor structural snapshots

Graphical abstract

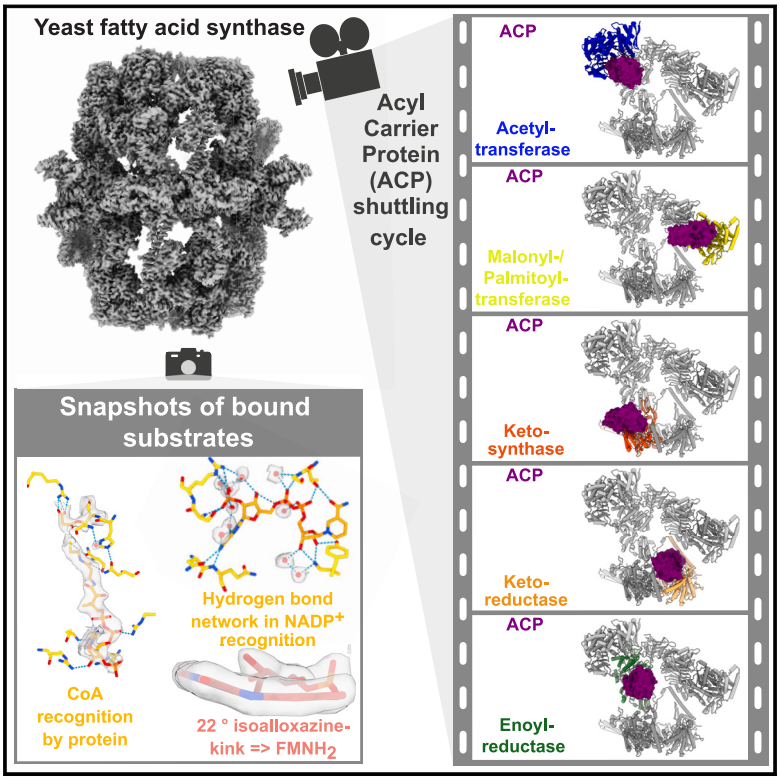

Highlights

- Yeast fatty acid synthase (FAS) structure at 1.9 Å resolution
- Structural snapshots of ACP representing intermediates in fatty acid biosynthesis
- Structural insight into cofactor recognition in FAS
- Direct modulation of the fatty acid profile output within the FAS reaction chamber

Authors

Kashish Singh, Georg Bunzel, Benjamin Graf, Ka Man Yip, Meina Neumann-Schaal, Holger Stark, Ashwin Chari

Correspondence

holger.stark@mpinat.mpg.de (H.S.), ashwin.chari@mpinat.mpg.de (A.C.)

In brief

Structural snapshots of cofactors in the yeast fatty acid synthase at 1.9 Å resolution and ACP structural snapshots representing intermediates in the fatty acid biosynthesis cycle open avenues for diversifying the product profile and discovering anti-fungal fatty acid synthase inhibitors.

Singh et al., 2023, Cell *186*, 5054–5067
November 9, 2023
https://doi.org/10.1016/j.cell.2023.10.009

CellPress

CellPress
OPEN ACCESS

Cell

Article

Reconstruction of a fatty acid synthesis cycle from acyl carrier protein and cofactor structural snapshots

Kashish Singh,[1,4] Georg Bunzel,[1,5] Benjamin Graf,[1,2,6] Ka Man Yip,[1,7] Meina Neumann-Schaal,[3] Holger Stark,[1,*] and Ashwin Chari[1,2,8,*]

[1]Department of Structural Dynamics, Max Planck Institute for Multidisciplinary Sciences, Am Fassberg 11, 37077 Göttingen, Germany
[2]Research Group Structural Biochemistry and Mechanisms, Max Planck Institute for Multidisciplinary Sciences, Am Fassberg 11, 37077 Göttingen, Germany
[3]Leibniz-Institut DSMZ-Deutsche Sammlung von Mikroorganismen und Zellkulturen GmbH, Inhoffenstrasse 7B, 38124 Braunschweig, Germany
[4]Present address: MRC Laboratory of Molecular Biology, Francis Crick Avenue, Cambridge Biomedical Campus, Cambridge CB2 0QH, UK
[5]Present address: ATEM SD GmbH, Buechelstr. 54, 42855 Remscheid, Germany
[6]Present address: Sartorius Lab Instruments GmbH & Co. KG, Otto-Brenner-Str. 20, 37079 Göttingen, Germany
[7]Present address: Thermo Fisher Scientific, De Schakel 2, 5651 GG Eindhoven, the Netherlands
[8]Lead contact
*Correspondence: holger.stark@mpinat.mpg.de (H.S.), ashwin.chari@mpinat.mpg.de (A.C.)
https://doi.org/10.1016/j.cell.2023.10.009

SUMMARY

Fatty acids (FAs) play a central metabolic role in living cells as constituents of membranes, cellular energy reserves, and second messenger precursors. A 2.6 MDa FA synthase (FAS), where the enzymatic reactions and structures are known, is responsible for FA biosynthesis in yeast. Essential in the yeast FAS catalytic cycle is the acyl carrier protein (ACP) that actively shuttles substrates, biosynthetic intermediates, and products from one active site to another. We resolve the *S. cerevisiae* FAS structure at 1.9 Å, elucidating cofactors and water networks involved in their recognition. Structural snapshots of ACP domains bound to various enzymatic domains allow the reconstruction of a full yeast FA biosynthesis cycle. The structural information suggests that each FAS functional unit could accommodate exogenous proteins to incorporate various enzymatic activities, and we show proof-of-concept experiments where ectopic proteins are used to modulate FAS product profiles.

INTRODUCTION

Fatty acid (FA) biosynthesis follows a sequential and repetitive enzymatic cycle employing acetyl-coenzyme A (CoA), malonyl-CoA, and NAD(P)H (Figure 1A).[1] The acyl carrier protein (ACP) and its post-translational activation on a serine residue by a phosphopantetheine (Ppant) prosthetic group (from CoA) are essential.[1] FA biosynthesis requires ACP-based active shuttling of biosynthetic acyl intermediates, acetyl-, and malonyl-groups, as covalent adducts to the Ppant group. In yeast, transacylases transfer the acetyl group of acetyl-CoA (acetyltransferase [AT] domain) or the malonyl group of malonyl-CoA (malonyl-palmitoyl-transferase [MPT] domain) onto the ACP. The acetyl group is first transferred onto the ketosynthase (KS domain) active site thiol, where it undergoes a condensation reaction with the ACP-bound malonyl group. The resulting Ppant-bound β-keto-acyl-ACP is reduced to β-hydroxy-acyl-ACP by the ketoreductase (KR domain) and transferred onto the dehydratase (DH domain). Dehydration of the Ppant-β-hydroxy-acyl to the α-enoyl-acyl-ACP and its reduction by enoylreductase (ER domain) result in a two-carbon atom elongated alkyl-acyl-ACP. The alkyl-acyl moiety is then transferred to the KS active site thiol, followed by another condensation reaction with MPT-activated malonyl-ACP. The cycle is then repeated until it yields a C16/C18 alkyl-acyl-ACP, which is transacylated to a free CoA molecule by the MPT domain.[2]

Despite this universally conserved biosynthetic cycle, two FA biosynthetic enzyme architectural solutions have evolved. Bacteria, plants, and mitochondria have independent FA synthase (FAS) enzymes and ACP (type II system).[3] Type II ACP relies on diffusion to interact with different enzymes. Second, integrated, large multi-subunit type I FAS systems exist.[4] Type I systems are either "X"-shaped dimers (α_2), typical of metazoan FAS, where each polypeptide contains all catalytic domains connected to the ACP through a flexible linker, or multimeric barrel-like structures, where all activities are unified on a single (α_6) in corynebacteria/mycobacteria/nocardia (CMN) bacterial FAS, or two ($\alpha_6\beta_6$) polypeptides in fungal FAS. These barrel-like

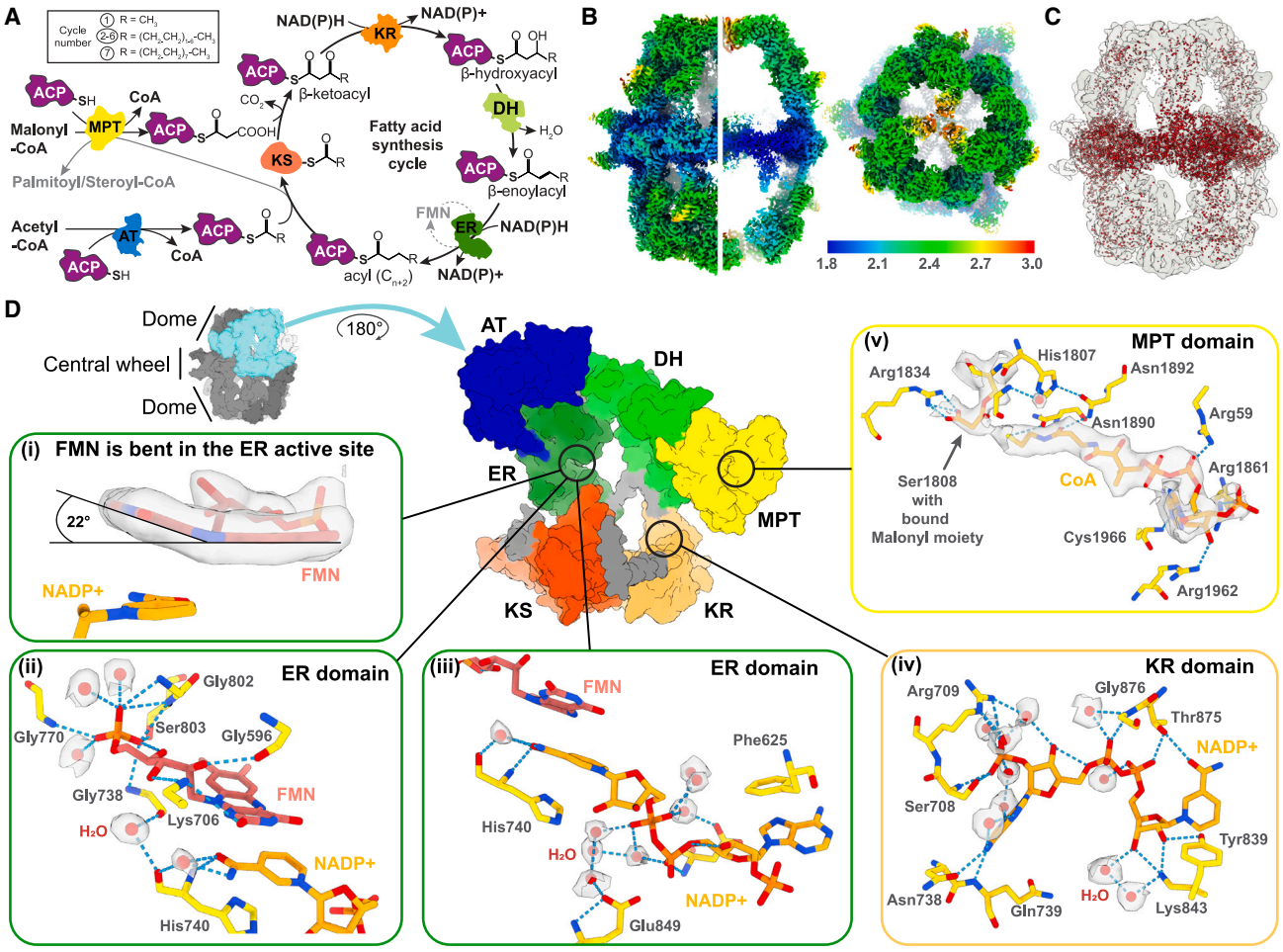

Figure 1. Structure of the *S. cerevisiae* FAS at 1.9 Å resolution

(A) The yeast fatty acid biosynthesis cycle is depicted. ACP, acyl carrier protein (purple); AT, acetyltransferase (blue); MPT, malonyl-palmitoyl-transferase (yellow); KS, ketosynthase (red); KR, ketoreductase (orange); DH, dehydratase (light green); ER, enoyl reductase (green); FMN, flavin mononucleotide.

(B) Local resolution map of the 1.9 Å FAS structure.

(C) Distribution of visualized water molecules in the 1.9 Å FAS structure.

(D) Visualized chemical details in the 1.9 Å structure. One of the six asymmetric units of FAS (indicated in cyan, top left) is extracted and depicted in the center. Individual enzymatic domains are colored following the same scheme as in (A). The locations of zooms (i–v) in the asymmetric unit are indicated. (i) FMN bound in the ER active site. The density indicates a 22° kink in the isoalloxazine ring system, consistent with its reductive role in FA biosynthesis. (ii) FMN recognition by ER active site amino acids and their accompanying water network. (iii) $NADP^+$ bound in the ER active site cleft with its nicotinamide group stacked between the FMN isoalloxazine and His740, a solvent network aids in recognition of the ADP moiety. (iv) Recognition of $NADP^+$ by amino acids and solvent in the KR active site cavity. (v) Malonyl-CoA was found in a post-hydrolysis state in the MPT active site. CoA interacts with many MPT active sites residues, while the malonyl group is covalently attached to Ser1808 and interacts with Arg1834.

Related to Figure S1.

structures are characterized by an equatorial central wheel with two domes emanating axially from the central wheel (Figure 1D). Here, the ACP resides within the FAS barrel, attached by two flexible linkers. The ACP in CMN and fungal FAS is extended by four helices (structural domain), in addition to the canonical four-helix bundle domain of bacterial and metazoan ACPs.[1,5] Type I FAS systems are thought to be efficient due to the compartmentalization of FA biosynthetic reaction chambers and the spatial proximity of catalytic sites.

Two potential logistical problems arise from the utilization of a common carrier protein to shuttle substrates and intermediates. (1) Hydrophobic ACP cargos need to be shielded from the polar cellular environment when in transit from one enzyme active site to another. In type II ACP, this is achieved by sequestration of bound intermediates into a hydrophobic cleft.[1] Upon arrival to the next enzyme, the ACP-acyl chain flips out of sequestration and extends into the active site in a "switchblade" mechanism.[6] (2) The common ACP surface and particularly its Ppant arm are promiscuous, but reduces the number of potential interaction sites to be sampled in specific recognition. In type II FA biosynthetic enzymes, for example, positively charged active site clefts interact with the negatively charged ACP α-helices 2 and 3.[1,6]

However, how these two logistical problems are addressed by type I FAS is unknown, primarily owing to sparse structural insight into ACP shuttling in type I systems.

ACP compartmentalization and the rapid transfer between individual enzyme-active sites could make switchblade sequestration unnecessary for fungal FAS. Although, NMR studies on isolated yeast FAS (yFAS) ACP domains indicate the potential for sequestration.[7,8] Conversely, the larger *S. cerevisiae* ACP engages in more extensive interactions. It binds to the AT and KS enzymatic domains using both canonical and structural ACP domains,[9–11] whereas the DH domain only binds the canonical domain.[12] Additionally, we reported two conformational states—rotated and non-rotated—adopted by *S. cerevisiae* β subunits that are associated with distinct spatial positions of ACP domains.[11] The non-rotated conformation correlated with ACP-KS domain binding, whereas the rotated conformation was consistent with ACP-AT domain binding, additionally stabilized by a newly discovered γ subunit. FA biosynthesis requires a cyclic, sequential, and ordered interaction of the ACP with six catalytic domains in total (Figure 1A). Two large-scale conformational rearrangements alone are probably insufficient for all these ACP interactions in the course of FA biosynthesis. Thus, one central question in FA biosynthesis is "How does conformational sampling in FAS affect ACP shuttling?" Although each ACP domain can theoretically access all active sites within a dome, MD simulations suggest ACP compartmentalization due to volume exclusion effects exerted by ACPs and their linkers.[13] Another central question in FA biosynthesis would then be, "How is ACP compartmentalization achieved?" Essential to answering these questions is to elucidate a series of structural snapshots of fungal FAS, revealing the ACP in all stages of the yeast FA synthesis cycle.

Herein, we precisely address this central requirement. We report cryo-electron microscopy (cryo-EM) structures of *S. cerevisiae* FAS with ACP domains bound to distinct enzymatic domains, representing different stages in FA biosynthesis. Employing technical advances in electron microscope (EM) optics,[14] we report a structure of FAS at 1.9 Å resolution, allowing the visualization of cofactors and solvent molecules. Structural ACP snapshots representing intermediate stages in FA biosynthesis could only be elucidated by image-processing procedures, which disentangle FAS into isolated functional compartments. The snapshots revealed that each FAS dome could accommodate additional exogenous proteins with a total mass of about 150 kDa per dome or 300 kDa per FAS. Incorporating a thioesterase into the FAS dome by using the γ subunit as a vector, we show that FAS product profiles can be directly modulated. Together, these findings represent the solid foundation to interrogate fungal FAS FA biosynthesis mechanisms in atomic detail and their biotechnological exploitation.

RESULTS

Structure of yFAS at better than 2 Å resolution

Initially, we sought technical advances to resolve *S. cerevisiae* FAS structures at a higher resolution than the presently attained 3 Å resolution structures. Particularly, a threshold better than 2 Å resolution is desirable, as the resulting density maps and models at this resolution are accurate with regards to side-chain rotamers and reveal many ordered solvent molecules and small ligands confidently. However, a survey of the PDB and the EMDB reveals that such resolutions are rarely attained for macromolecules larger than 1 MDa (such as FAS), and only a handful of entries exist. To be able to cross this threshold, we decided to reduce potential structural heterogeneity by employing FAS purified from a *S. cerevisiae* strain with a chromosomally deleted γ subunit (Δγ-FAS).[11] Δγ-FAS was additionally conformationally stabilized by incubation with saturating concentrations of malonyl-CoA and $NADP^+$ prior to cryo-EM grid preparation. EM grids were imaged using a 300 kV Titan Krios Mono/BCOR microscope,[14] resulting in a dataset with an experimental B-factor of ∼53 $Å^2$, yielding a structure at a nominal resolution of 1.9 Å (Figures 1B and S1; Table S1). The local resolution of the map varied from 1.8 to 2.2 Å at the central wheel to 2.2–2.7 Å at the dome region (Figures 1B and S1E). This spread in local resolution has been observed earlier.[11,15] Notably, optical improvements in the EM proportionally allow higher resolution to be attained, which is almost ∼1 Å better than any previously reported structure of yFAS.

In the structure, ∼7,700 water molecules were confidently modeled, representing an average of 0.33 water molecules per residue (∼0.48 water at the central wheel and ∼0.18 water in the dome per residue) (Figure 1C). The added resolution reveals a 22° kink in the isoalloxazine ring system of flavin mononucleotide (FMN) in the ER active site (Figure 1Di) that eluded observation in earlier structures (Figure S1H).[11,15–18] This isoalloxazine kink indicates that FMN is in its reduced form, consistent with the reductive function of ER in FA biosynthesis (Figure 1A). A hydrogen bonding network involving both side chains and water molecules stabilizes FMN within the ER active site (Figure 1Dii). Similarly, polar contacts involving both amino acid side chains and water molecules enable $NADP^+$ recognition in both the ER and KR active sites (Figures 1Diii, 1Div, and S1I). The map is in agreement with a MPT active site nucleophile Ser1808-Oγ malonic acid ester and a bound post-hydrolysis CoA molecule (Figure 1Dv). Owing to the lower local resolution at the MPT, very few localized water molecules could be placed.

Visualizing ACP domains in positions representing intermediates in FA biosynthesis

All six FAS ACP domains have been observed bound to the KS domain in biochemically synchronized samples, achieved by chasing FA synthesis intermediates by incubating FAS with saturating amounts of malonyl-CoA and NADPH (Figure 2Ai, left).[9,11] Starting from this "cycled" state, incubation of FAS with saturating γ subunit concentrations has afforded AT-bound ACP domain stabilization with FAS domes in the rotated conformation (Figure 2Ai, right).[11] These two ACP states were observed irrespective of the symmetry imposed in cryo-EM reconstructions. However, in the 1.9 Å FAS structure (Figure 1), ACP domains were poorly defined and essentially unresolved. We hypothesized that this is a consequence of biochemical heterogeneity within the FAS dome, in the form of ACP domains occupying non-identical positions in each functional compartment. Should this indeed be the case, one would either expect that

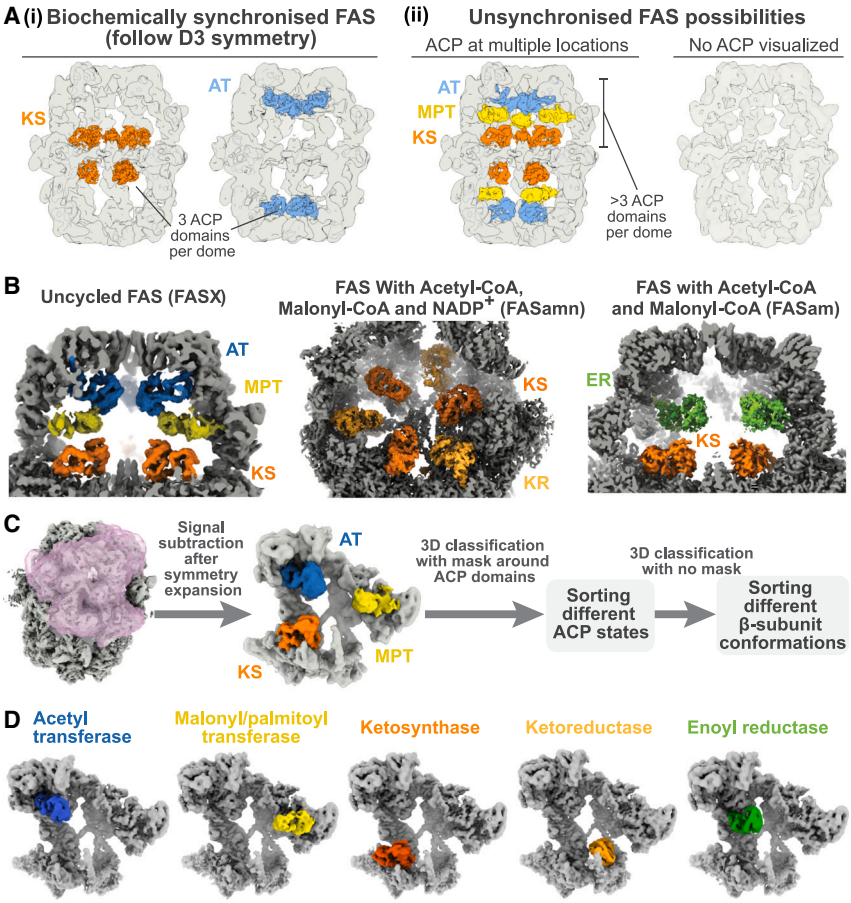

Figure 2. Visualizing ACP domains in positions representing intermediates in fatty acid synthesis

(A) (i) Only three unique ACP densities are visualized in each dome of biochemically synchronized FAS. (ii) Two scenarios are conceivable in unsynchronized FAS: either ACP domains remain unresolved (right) or densities greater than three are visualized (left). Both scenarios would imply asynchronous binding of the three ACP domains to different enzymatic domains within a FAS dome.

(B) Distribution of ACP domains in uncycled FAS (FASx, left), FAS in the presence of acetyl-CoA, malonyl-CoA, $NADP^+$ (FASamn, middle), and FAS in the presence of acetyl-CoA and malonyl-CoA (FASam, right).

(C) Image-processing scheme for sorting different ACP-bound states.

(D) Structures of FAS asymmetric units with ACP visualized in positions representing five intermediates in FA biosynthesis as indicated.

Related to Figures S2 and S3.

no/fragmented ACP densities are observed, similar to the situation in the high-resolution FAS structure (Figures 1 and 2Aii, right), or that more than three partial ACP densities are observed in a dome (Figure 2Aii, left). The ACP domain is an integral part of the α subunit, and thus, biochemically, no more than three can exist in a FAS dome. Both scenarios would indicate imprecise averaging of single particle images in image processing when reconstructing the FAS structure. Overcoming these challenges of biochemical heterogeneity, combined with solutions to these technical cryo-EM challenges, would yield structural information, albeit at a lower resolution, about interesting functional intermediates in the FA biosynthetic cycle. In the following, we describe how we have partially been able to overcome these image processing challenges.

Non-uniform ACP binding to various active sites within a single FAS dome is most likely the reason why ACP remains poorly resolved. To verify this, we first determined the FAS structure (without imposing symmetry) that had not been chased by malonyl-CoA and NADPH ("uncycled," referred to as "FASx" hereafter). We expected ACPs to be most randomly distributed within the FAS dome in this case. In agreement, the FASx structure displayed nine low-threshold, partial ACP densities per dome or eighteen per FAS adjacent to AT, MPT, and KS (Figures 2B, left, and S2A). Asymmetric structures of cycled FAS incubated with acetyl-CoA, malonyl-CoA, and $NADP^+$ (hereafter referred to as FASamn) displayed six partial ACP densities per dome or twelve per FAS juxta-posed to KR and KS (Figures 2B, middle, and S2B). Cycled, asymmetric FAS structures with acetyl-CoA and malonyl-CoA (hereafter referred to as FASam) revealed six partial ACP densities per dome or twelve per FAS residing next to ER and KS (Figures 2B and S2C).

Visualizing more than three ACP domains within FAS domes as discussed indicates an averaging-out effect of protein densities by image processing. In FAS, the larger, pseudo-symmetric barrel structure appears to mainly drive image alignments and not ACP domains, which leads to this ACP density loss in reconstructions. To overcome this obstacle, a strategy involving initial three-dimensional (3D) refinement imposing strict D3 symmetry, followed by symmetry expansion and particle signal subtraction[19,20] was pursued to *in silico* extract the six $\alpha\beta$ dimers (asymmetric unit) from each FAS particle. FAS asymmetric units were then classified using masks representing a single ACP position, followed by classification without any mask (Figures 2C and S2A–S2C). This resulted in asymmetric unit structures of ~3 Å resolution, revealing full, single-position ACP densities (Figures S2D and S3), representing intermediate stages in FA biosynthesis (Figure 2D).

FAS conformations and modes of ACP binding to enzymatic domains

FAS β subunits have been previously shown to adopt two major conformations—non-rotated and rotated.[9–11,21] In FASx and FASam datasets, two additional hybrid conformational states were identified. In the semi-non-rotated (SNRot) state, AT and ER domains are in a non-rotated conformation, whereas DH and MPT domains adopt rotated conformations (Figure 3A; Video S1). The semi-rotated (SRot) state is characterized by a

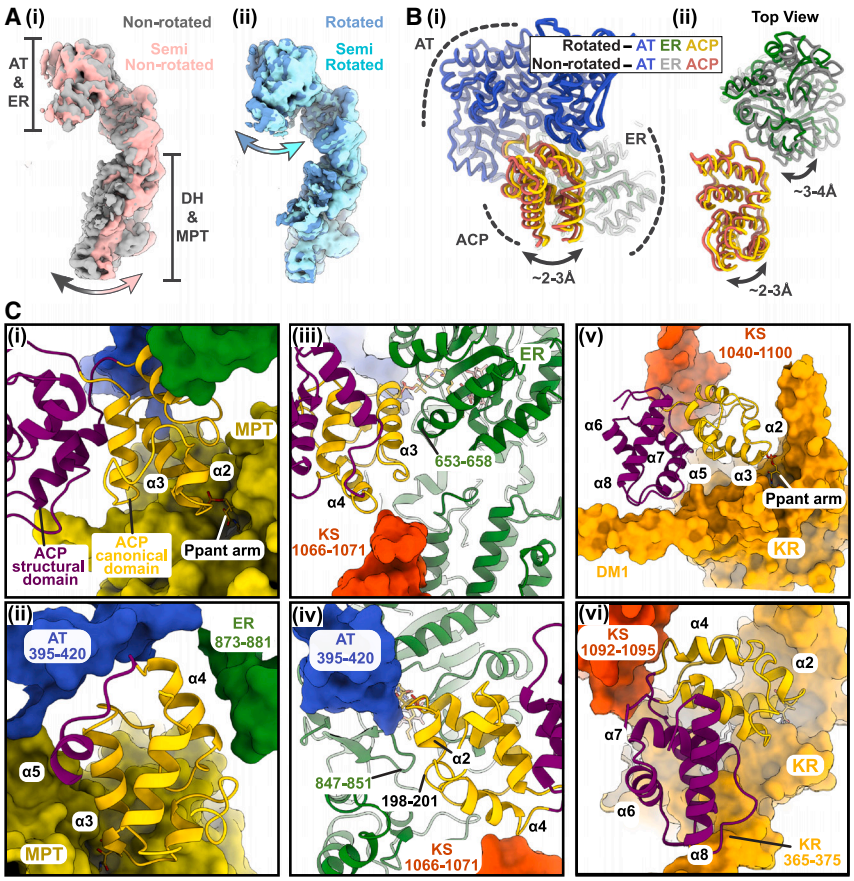

Figure 3. ACP-FAS enzymatic domain interactions

(A) (i) Overlay of non-rotated and semi-non-rotated states. The major difference lies in the DH and MPT domains that are rotated outward in the semi-non-rotated state. (ii) Overlay of rotated and semi-rotated states. These two states differ in AT and ER domains that are only partially rotated in the semi-rotated FAS state.

(B) Overlay of AT domain-bound ACP in rotated and non-rotated FAS asymmetric units. Aligning AT domains reveals that the ACP pivots around Ser180 to position itself between AT and ER.

(C) Interactions of the ACP when bound to MPT (i and ii), ER (iii and iv), and KR domains (v and vi). ACP helices α2, and α3 contact residues outside the MPT active site cleft (i), whereas helix α4, and the loop between helix α4/5 contact structural segments of the ER (874–880) and AT (402–406) domains, respectively (ii). At the ER domain, ACP helix α3 contacts the ER loop (653–658), whereas helix α4 lies adjacent to the structural segments (1066–1071) of the KS domain (iii). Furthermore, ACP helix α2 contacts the adjacent AT segment (402–407), whereas ACP residues (198–201) are proximal to an ER loop (residues 847–851) (iv). At the KR domain, both canonical and structural ACP domains are involved in binding. ACP helices α2 and α3 contact residues near the KR active site (v), whereas the structural domain rests upon the DM1 helix contacting residues 365–375 (vi). The ACP loop between helix α4/5 also forms contacts with the adjacent KS residues 1092–1095 (vi).

Related to Figures S2, S3, S4, S5, S6, and S7.

largely rotated conformation, with the AT domain not fully rotated (Figure 3A; Video S1). The ACP was found to be AT domain-adjacent in all four β subunit conformations, which can be explained by its ability to pivot about Ser180 (Figure 3B; Video S2). This ACP swivel allows it to adapt to the space between AT and ER in different conformations while maintaining interactions through canonical and structural domains. ACP positioned at KS and ER was correlated with non-rotated and SNRot conformations only, consistent with small changes in both domains in these conformations. ACP-KR binding, however, only correlated with non-rotated conformations. In addition, DH-bound ACP[12] was found in a non-rotated state. These findings suggest that the rotated β subunit conformation is exclusive to the acetyl loading step, whereas the condensation and elongation phases appear to occur in the non-rotated conformation. Therefore, these new conformations are likely adopted when ACP is in transit from AT to KS and vice versa.

The snapshots captured herein, and in earlier studies,[9,11,12] allow addressing which determinants are exploited by FAS enzymatic domains to recognize the ACP. The ACP canonical domain that includes Ppant-Ser180 and its flanking α-helices 2 and 3 is positioned at the active site cleft openings of MPT, KR, and ER domains (Figure 3C). ACP canonical domain recognition appears predominantly electrostatic, consistent with the charge complementarity of the interaction surfaces (Figure S4). These interactions resemble ACP canonical domain KS, AT, and DH domain associations[9,11,12] and therefore appear to be universally conserved in ACP canonical domain-active site interactions. For MPT-, KR-, and ER-bound ACP, we mapped additional ACP-FAS interactions (Figure 3C): ACP also contacts nearby structural elements of AT and ER through ACP helix α4 at the MPT (Figures 3Ci and 3Cii). At the ER, residues of ACP α-helices 2 and 3 along with the loop joining helices α3/4 form extensive contacts, and the nearby structural elements of the AT and KS interact with ACP helices α2 and α4, respectively (Figures 3Ciii and 3Civ). At the KR, ACP helices α2 and α3 contact KR residues outside the active site, whereas the loop between ACP helices α3/4 recognizes nearby structural elements of the KR, and ACP helix α4 interacts with the KS (Figures 3Cv and 3Cvi). Unlike ER and MPT, the KR-bound ACP forms additional contacts with the KR domain coiled-coil dimerization segments using its yeast-specific extension (helix α5, loop between helices α5/6 and helices α7/8).

Thus, findings in Figures 3B and 3C, along with those previously reported[9,11,12] infer that structural elements distant from active sites are generally involved in ACP binding. Furthermore, the yeast-specific ACP structural domain mediates interactions when bound to KS, KR, and AT. The canonical ACP domain, however, is universally required for interaction with all enzymatic domains of FAS.

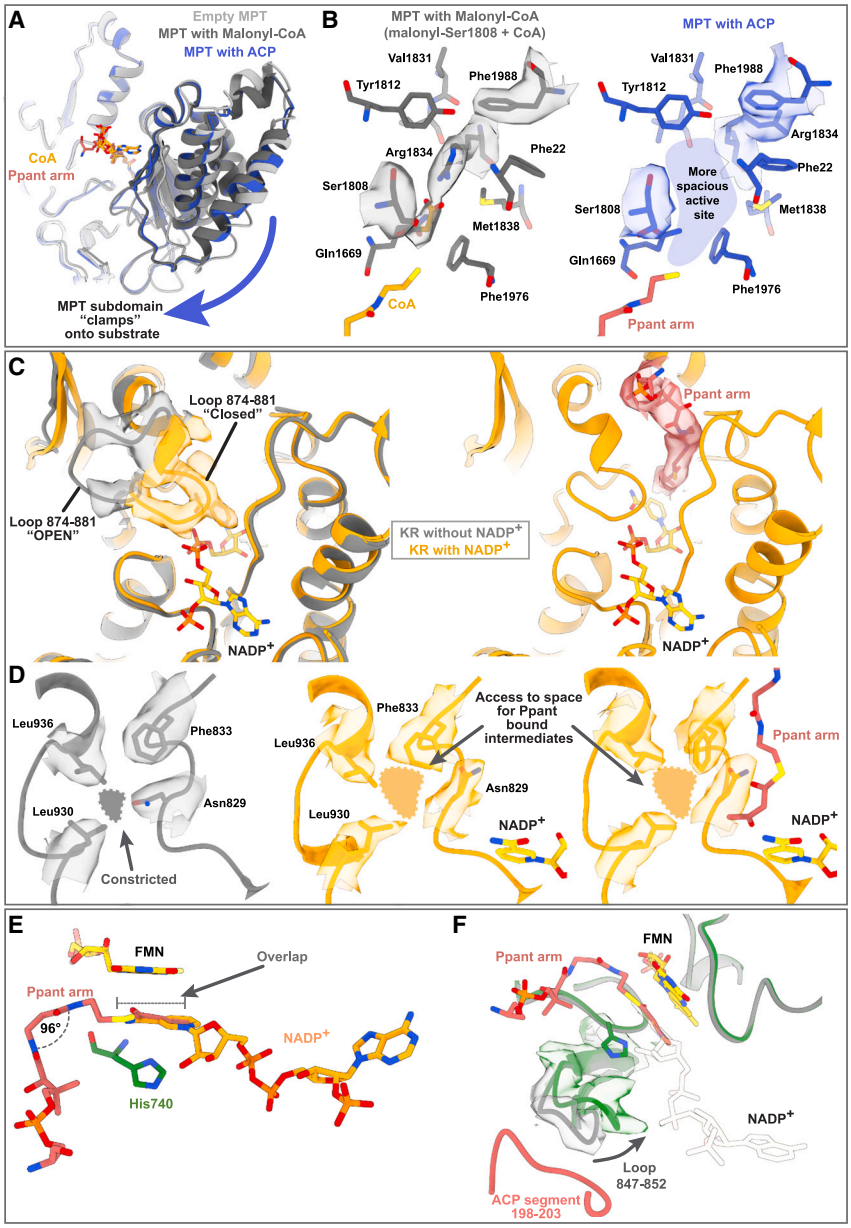

Figure 4. Structural rearrangements upon substrate and ACP binding

(A) Overlay of empty (light gray), malonyl-CoA-bound (dark gray), and ACP-bound (blue) MPT domains.

(B) MPT active site comparison in the presence of malonyl-CoA (left) and in the ACP-bound state (right).

(C) Overlay of the KR active site in the presence (orange) and absence (gray) of $NADP^+$.

(D) KR active site in the absence of $NADP^+$ (left), with bound $NADP^+$ (middle), and $NADP^+$ and ACP together (right).

(E) Overlay of Ppant arm and $NADP^+$ at the ER, depicting the mutually exclusive binding of these two entities as a consequence of a steric clash.

(F) Overlay of the ER active site with bound $NADP^+$ (gray) and bound ACP (green). The loop 847–852 is shifted inward when ACP is bound, resulting in a narrower ER active site cleft.

Related to Figures S2, S3, S5, and S6.

Structural changes to accommodate the Ppant arm in MPT, KR, and ER domains

We next addressed the question of whether local conformational adaptations of MPT, KR, and ER domains aid in ACP, and in particular Ppant arm, recognition. We have been able to capture two different variations of the Ppant-group bound to MPT: the first stems from malonyl-CoA as an isolated molecule (Figure 1D), and the other is where the Ppant group is covalently attached to the ACP Ser180 (Figure S2Di). In both cases, a large conformational change is observed, characterized by a movement of the MPT helical subdomain toward the MPT catalytic Ser1808 (Figure 4A). The result is the enclosure of Ppant in a clamp-like manner. The overall MPT active site cavity expands in the ACP-bound state and could explain how malonyl-CoA or malonyl-ACP are distinguished from longer ACP-bound acyl intermediates (Figure 4B, right). At present, this explains the accommodation of Ppant-acyl adducts of up to 10 carbon atoms (~16 Å) but leaves open the question of how palmitoyl- or stearoyl-acyl adducts could bind.

Similarly, two scenarios of the $NADP^+$-bound KR domain were captured in this manuscript: in the absence of an ACP-bound Ppant arm (Figure 1Div) and its presence (Figure 3C). In both scenarios, closure of a loop on the nicotinamide-ribose moiety of $NADP^+$ was observed (Figure 4C), similar to what has been reported previously.[22] The loop closure creates a pocket that represents an entry site for the ACP-bound Ppant arm and fulfills a dual purpose: stabilization of NADPH/$NADP^+$ binding and the ACP-bound Ppant arm (Figure 4C). NADPH/$NADP^+$ binding also causes the expansion of a constriction lined by Asn829, Phe883, Leu930, and Leu936, allowing the KR active site to accommodate fatty acyl intermediates longer than 4–6 carbon atoms (Figure 4D).

In the ER, the Ppant arm enters the active site through a cleft within the FAS dome. Strikingly, the Ppant arm is kinked by ~96° in the ER active site (Figure 4E), allowing the enoyl bond to be positioned between the catalytic His740 and FMN. The present resolution of the structure does not allow distinguishing a *cis*- or *trans*-enoyl bond, but both could be accommodated in this position (Figure S2Div). Superposition of the ACP-bound ER domain (Figure 3C) with the $NADP^+$-bound ER domain (Figure 1Diii) reveals that nicotinamide and the enoyl-ACP Ppant-arm adduct would occupy the same position adjacent to the FMN isoalloxazine (Figure 4E). Accompanying this, when ACP-bound, an ER loop segment constricts the adenosine

diphosphate phosphoribosyl (ADPR) binding cleft by ~3 Å, making NADPH/NADP$^+$ and enoyl-acyl-ACP binding mutually exclusive (Figure 4F).

Taken together, an ACP-Ppant-mediated motion in the MPT and a NADPH/NADP$^+$-mediated loop closure in the KR result in a clamping motion that allows Ppant-arm recognition and the accommodation of covalent acyl intermediates of ever-increasing length in FA biosynthesis. In contrast, a pre-formed cleft is exploited in the ER for the positioning of a kinked enoyl-Ppant arm over the isoalloxazine ring of FMN, which constricts the active site to render enoyl-acyl-ACP binding mutually exclusive to NADPH/NADP$^+$.

Comparison of ACP-FAS enzyme interactions in type I and type II systems

The elucidation of yeast ACP (yACP) domain structures bound to several yeast FAS (yFAS) enzymatic domains in this manuscript and earlier,[12] allows for the comparison of ACP recognition by FAS enzymes in type I and type II systems. For this, the structure of ACP bound to the malonyl-CoA-ACP transacetylase (MCAT) enzyme (PDB: 6U0J)[23] with yACP-bound yFAS-AT (Figure S5A) and yACP-bound yFAS-MPT (Figure S5B) structures was compared, as the MCAT serves both transacylase functions in bacteria. Furthermore, the FabB KS structure bound to ACP (PDB: 6OKC)[24] is compared with the yACP-bound yFAS KS (PDB: 6QL9;[11] Figure S5C), and the FabB DH bound to ACP (PDB: 4KEH)[6] is compared with the yACP-bound yFAS-DH (PDB: 6WC7;[12] Figure S5D).

The bacterial ACP, AcpP, interacts with MCAT through α-helix 2 (corresponds to α-helix 3 in yACP) and the α2/3 loop, the interaction interface yielding a buried surface area (BSA) of 459 Å^2 (Figures S5Aii and S5Bii). In yFAS-AT, additional structural segments exist in addition to the conserved catalytic domain (Figure S5Ai, left). Although the Ppant-Serine is similarly positioned at the opening of the active site cleft in bacterial and yFAS structures (Figure S5Ai, right), the AcpP-like binding pose is not possible in the yFAS-AT due to clashes with the yFAS-AT structural loop and adjacent ER domain segments (Figure S5Aiii). Instead, yACP α-helices 2 and 3 (BSA 530 Å^2) interact with the AT catalytic domain, the yACP loop α3/4 contacts adjacent ER segments (BSA 240 Å^2), and yACP α-helix 5 associates with the AT structural domain (BSA 263 Å^2) in yFAS-AT. Thus, the yACP:yFAS-AT interaction interface has nearly doubled in comparison to MCAT-AcpP.

The yFAS-MPT also has structural segments that are additional to the catalytic domain (Figure S5Bi). yACP interacts with yFAS-MPT through its α-helix 3 (BSA 238 Å^2), and its α-helices 4 and 5 to adjacent structural segments of ER- and AT domains (BSA 216 Å^2) (Figure S5Biii). Thus, the interaction surface of yACP has been redistributed with regards to AcpP to incorporate the yACP structural domain and exploit neighboring segments of the yFAS architecture while maintaining a similar interaction interface magnitude.

Both bacterial and yFAS KS are homodimers, the latter containing additional structural segments (Figure S5Ci). AcpP interacts through its α-helices 2 and 3 with FabB (BSA 803 Å^2) (Figure S5Cii). The yACP exploits α-helix 3 in a different pose than AcpP α-helix 2 to interact with the KS catalytic domain (BSA 377 Å^2) and uses α-helices 5 and 6 to interact with KS structural segments (BSA 477 Å^2) (Figure S5Ciii). However, again, the magnitude of the yACP interaction interface is maintained in comparison to AcpP while employing the yACP structural domain and KS structural segments.

FabA forms a dimer, whereas yFAS-DH has pseudo-dimeric organization (Figure S5Di). AcpP α-helix 2 is primarily involved in FabA binding (Figure S5Dii); similarly, yACP α-helix 3 is primarily involved in DH interaction (Figure S5Diii). However, as expected by the architectural differences between yFAS-DH and FabA, the yACP binding pose at yFAS-DH is distinct from AcpP FabA binding. Most likely, this different binding pose is due to DH structural elements and the adjacent ER domain.

No AcpP structures exist bound to bacterial KR and ER enzymes; we have therefore restricted ourselves to comparing the overall architecture and co-substrate binding to the fungal-like ER FabK (PDB: 4IQL;[25] Figure S6A) and KR FabG (PDB: 1Q7B;[26] Figure S6B).

yACP interacts with yFAS-ER mainly through its canonical domain (BSA 701 Å^2), and some sparse contacts to its structural domain (BSA 69 Å^2). Both FabK and yFAS-ER have an extended active site cleft with two entrances A and B (Figures S6Ai and S6Aii). In yFAS-ER, NADPH/NADP$^+$ enters the active site cleft through entrance B (Figure S6Aiii), whereas the yACP Ppant arm enters through entrance A (Figure S6Aiv). Considering that the ADP moiety of NADPH/NADP$^+$ adopts a similar position at entrance B in FabK as in yFAS-ER (Figures S6Av and S6Avi), and a competitive inhibitor of FabK occupies the Ppant-arm binding site at entrance A (Figures S6Avii and S6Aviii), ACP recognition is likely to be conserved in both systems.

FabG is tetrameric, whereas the yFAS-KR dimerizes, and the catalytic fold between type I and type II systems is well conserved (Figures S6Bi and S6Bii). NADP$^+$-bound FabG (Figure S6Biii) resembles apo yFAS-KR (Figure S6Biv), which is much more open than NADP$^+$-bound yFAS-KR (Figures 4C and S6Bv). As NADP$^+$ and the catalytic tyrosine residue superpose well in both FabG and yFAS-KR, the AcpP-Ppant arm in FabG could occupy a similar position as in yFAS-KR (Figures 4C and S6Bvi). Furthermore, the FabG active site cleft is more open and could easily accommodate long fatty acyl chains.

Apparent asynchrony in ACP shuttling among various functional compartments

Within this manuscript, we used procedures where we extracted asymmetric units of FAS to overcome limitations in image processing of the entire FAS (Figures 2C and S2A–S2C). This has enabled the analysis of ACP and Ppant-arm recognition by enzymatic domains, along with accompanying large- and small-scale conformational changes (Figures 3 and 4). However, considering that 6 functional compartments form an intricate, interwoven FAS assembly, it would be desirable to know the spatial relationships between asymmetric units.

For this, we tallied ACP domain positions in asymmetric units of the individual datasets (Figures S2A–S2C; Table S2) and corresponding β subunit conformations (Figure 5A). The FASx dataset contained particles in overall rotated (FASx$_R$) and non-rotated conformations (FASx$_{NR}$), whereas FAS particles in the

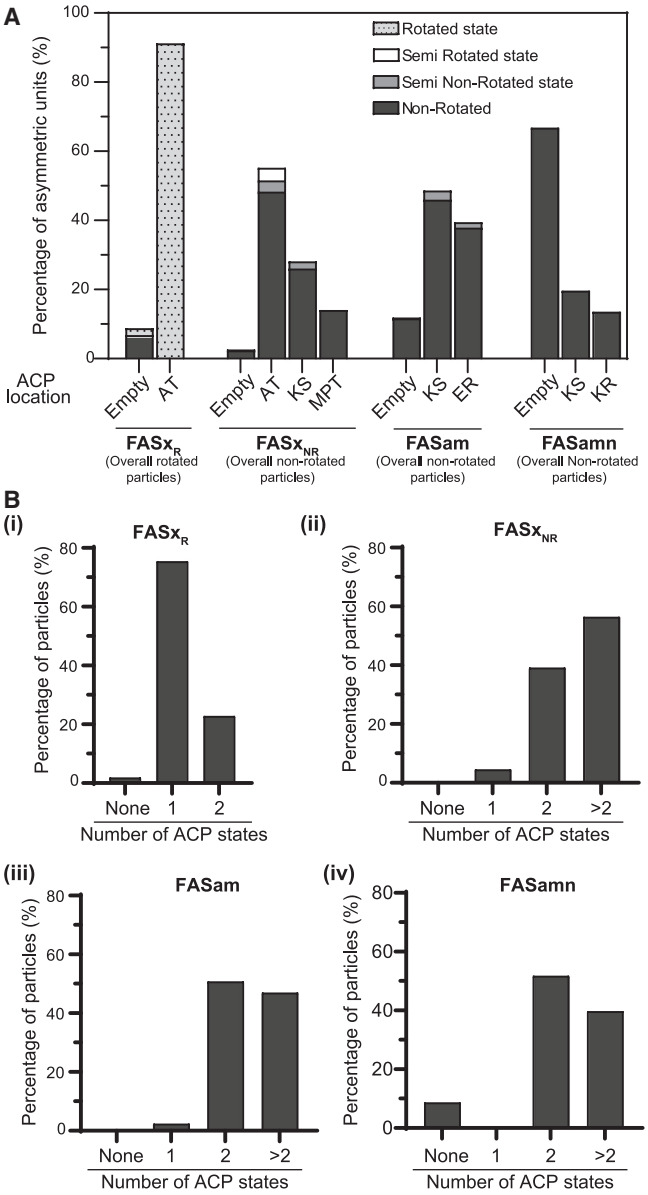

Figure 5. Asynchronous distribution of ACP in various functional compartments

(A) ACP distribution in correlation to FAS asymmetric unit conformation.

(B) ACP domain distribution in entire FAS particles of the FASx dataset. (i) Particles with an overall rotated conformation, (ii) particles with overall non-rotated conformation, (iii) ACP domain distributions in entire FAS particles of FASam, and (iv) FASamn, respectively.

Related to Figures S2 and S3.

FASamn and FASam datasets exclusively resided in an overall non-rotated conformation. Most asymmetric units of $FASx_R$ particles had ACP bound to the AT domain, whereas some asymmetric units had unresolved ACP domains and were empty. In the $FASx_{NR}$ pool, half the asymmetric units had AT-bound ACPs, the majority adopting a non-rotated β subunit conformation, whereas 12% of this subset adopted SRot and SNRot conformations. The remaining asymmetric units of the $FASx_{NR}$ pool had ACPs bound to the KS domain (28%), the MPT domain (14%), or were empty (3%). Some $FASx_{NR}$ asymmetric units with KS-bound ACP adopted SNRot, in addition to non-rotated conformations, whereas MPT-bound ACP only correlated with the non-rotated conformation. In the FASam pool of asymmetric units, almost half had KS-bound ACPs, 40% had ER-bound ACPs, and 12% were empty. Conversely, in the FASamn pool, 20% of the asymmetric units had KS-bound ACP domains, whereas 14% of the ACPs were KR-bound, and 66% of the asymmetric units were empty.

Next, we traced all asymmetric units back to the original FAS particles, employing the rotational matrix computed to extract the asymmetric units.[27] After this *in silico* reassembly of FAS particles, ACP locations were mapped based on overall dome conformations prior to extraction of asymmetric units (Figure 5B). FAS particles in the $FASx_R$ pool show that 75% of FAS particles have six AT-bound ACPs, and 23% mostly have AT-bound ACPs and at least one unresolved ACP (Figure 5Bi). In all FAS particles reconstructed from the three other asymmetric unit pools ($FASx_{NR}$, FASam, and FASamn), less than 5% appear to contain a singular ACP domain position. About half the reconstructed FAS particles contained ACPs in at least two distinct positions, whereas in the other FAS particles, ACPs are found in more than two states or are not resolved at all (Figures 5Bii–5Biv).

We conclude that the rotated state is the most homogeneous with respect to ACP domain location (at the AT domain) and that condensation and elongation cycles proceed in non-rotated β subunit conformations. In the presence of all 3 co-substrates, ACP domains appear to move either asynchronously or remain unresolved. This might indicate the ACP domain's ability to sample many more positions than just those adjacent to enzymatic domain-active sites when all co-substrates are present.

Exploitation of ACP structural snapshots in the FA biosynthesis cycle to re-engineer FAS

Structures of yACP bound to several yFAS enzymatic domains potentially provide a route to re-engineer the FA biosynthetic output of yFAS. Importantly, mapping the *Y. lipolytica* (an oleaginous, biotechnologically relevant yeast) FAS sequence onto the structural snapshots obtained in this manuscript reveals that all ACP and enzymatic domain amino acids involved in mutual interaction are conserved (Figure S7). The free internal volume within the FAS barrel considering all ACP positions and yFAS conformations is estimated to be ~3.9 × 10^5 Å^3, reduced to ~ 3.6 × 10^5 Å^3 by binding of 6 γ subunits, suggesting that each yFAS dome can accommodate up to about 150 kDa (300 kDa for total FAS) of additional exogenous globular proteins. As the γ subunit resides with the FAS dome and binds in a specific manner, it can be exploited as a vector.[11]

We performed a proof-of-concept experiment to address the feasibility of this (Figure 6A). Δγ-FAS was reconstituted with either the γ subunit alone or the following proteins replacing γ subunit residues 114–132: 1 copy of the fluorescent protein UnaG (γ-1xUnaG; 30 kDa), 2 head-to-tail copies of UnaG (γ-2xUnaG; 45 kDa), *V. harveyi* thioesterase TesA (γ-Tes; 50 kDa), or *V. harveyi* TesA not incorporated into the γ subunit scaffold as a control (Tes). Due to the widely differing molecular weights of these proteins and the 2.6 MDa yFAS, the reconstitution

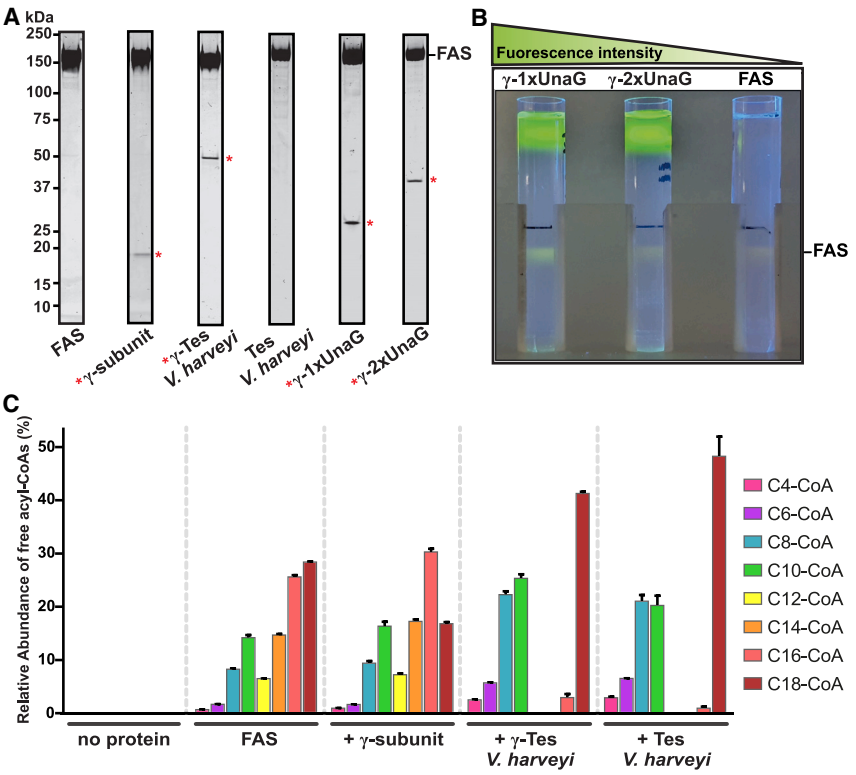

Figure 6. Exogenous enzyme activities directly re-engineer the fatty-acyl-CoA output of FAS

(A) SDS-PAGE of peak gradient fractions of FAS reconstituted with various proteins. From left to right, these are: FAS (buffer addition only), γ subunit (wild type), γ-Tes *V. harveyi*, Tes *V. harveyi* (*V. harveyi* TesA alone), γ-1xUnaG, or γ-2xUnaG. The respective proteins reconstituted with FAS are denoted with red asterisks.

(B) Efficiency of reconstitution can be monitored by additional fluorescence intensity. Shown are three density gradients after sedimentation (γ-1xUnaG left, γ-2xUnaG middle, FAS alone right). Note that both γ-1xUnaG and γ-2xUnaG increase the intrinsic FMN fluorescence of FAS alone.

(C) Relative abundance of free acyl-CoAs in the absence of protein (no protein; left), Δγ-FAS (FAS; 2nd from left), FAS bound to the γ subunit (+ γ subunit, middle), FAS bound to γ subunit-TesA fusion protein (+ γ-Tes *V. harveyi*; 2nd from right), and Δγ-FAS subsequently treated with TesA (+ Tes *V. harveyi*; right) as measured by LC/MS. Note that C12-CoA and C14-CoA are absent when FAS is bound to γ subunit-TesA fusion protein; C16-CoA is markedly reduced, whereas the relative abundance of C8-CoA and C10-CoA is increased (2nd from right). This can be attributed to thioesterase activity, as a Δγ-FAS reaction subsequently treated with TesA shows a similar product profile (right) and argues that C12, C14, and C16 are present as free fatty acids and therefore not detected in LC/MS. All measurements were performed in triplicate (n = 3), and the error bars for the relative abundance of the individual species are indicated.

mixture was fractionated by sucrose-density centrifugation. Proteins co-sedimenting with yFAS in high-molecular-weight fractions were assumed to be bound. All proteins, when incorporated into the γ subunit vector, bound to Δγ-FAS, but notably, Tes alone did not (Figure 6A). In the case of γ-1xUnaG and γ-2xUnaG, a substantial increase relative to the intrinsic FMN fluorescence of Δγ-FAS was seen (Figure 6B). Finally, by liquid chromatography/mass spectrometry (LC/MS), we were able to verify that Δγ-FAS reconstituted with γ-Tes exhibited a different acyl-CoA product profile in comparison to Δγ-FAS alone or Δγ-FAS reconstituted with the γ subunit (Figure 6C). Notably, the acyl-CoA product profile of Δγ-FAS reconstituted with γ-Tes exhibited a markedly higher abundance in C8- and C10-CoA and a lower abundance in C12-, C14-, and C16-CoA. As a Δγ-FAS reaction subsequently treated with *V. harveyi* TesA displayed a similar product profile, we attribute this product profile change to the thioesterase specificity within the FAS dome. Together, we have demonstrated that knowledge about yACP structural snapshots can inform ways to modulate yFAS product profiles in oleochemical production.

DISCUSSION

In this manuscript, we have elucidated enzymatic domain-bound ACP snapshots, representing functional intermediates in the yeast FA biosynthesis cycle. These include AT-, KS-, MPT-, KR-, and ER-bound ACP states, as well as substrate-, co-substrate-, and cofactor-bound states. For AT-, MPT-, KR-, and ER-bound ACP domains, we were able to resolve the functionally essential Ppant arm that enables the shuttling of starter chemical groups, biosynthetic intermediates, and products as covalent adducts from one active site to the other. This has allowed us to investigate modes of ACP- and Ppant-arm recognition in distinct functional states and the structural consequences thereof. Together, the reported findings, along with those previously reported,[9,11,12] allow us to reconstruct a complete architectural framework of transitions in the FA biosynthetic cycle (Figure 7A; Video S3). These snapshots suggest that each FAS dome could accommodate exogenous proteins, 150 kDa in mass. Proof-of-concept experiments show that such exogenous proteins could be used to modulate FAS product profiles. This framework represents the solid foundation to interrogate FA biosynthesis mechanisms at atomic resolution, develop activity-based and biophysical probes, aid in rational inhibitor design, and modify and exploit its function in oleochemical production.

High-resolution structure determination of type I FAS using cryo-EM

A pre-requisite to gain functional mechanistic insights and establish structure-function relationships is a detailed and accurate description of enzyme-active sites and their structural changes in functional states. This entails the protein backbone and side chains, prosthetic groups, co-substrates, and the ordered solvent (waters and ions) of the macromolecular complex. Although all these features are identifiable at different resolution thresholds, ordered solvent can be accurately described at

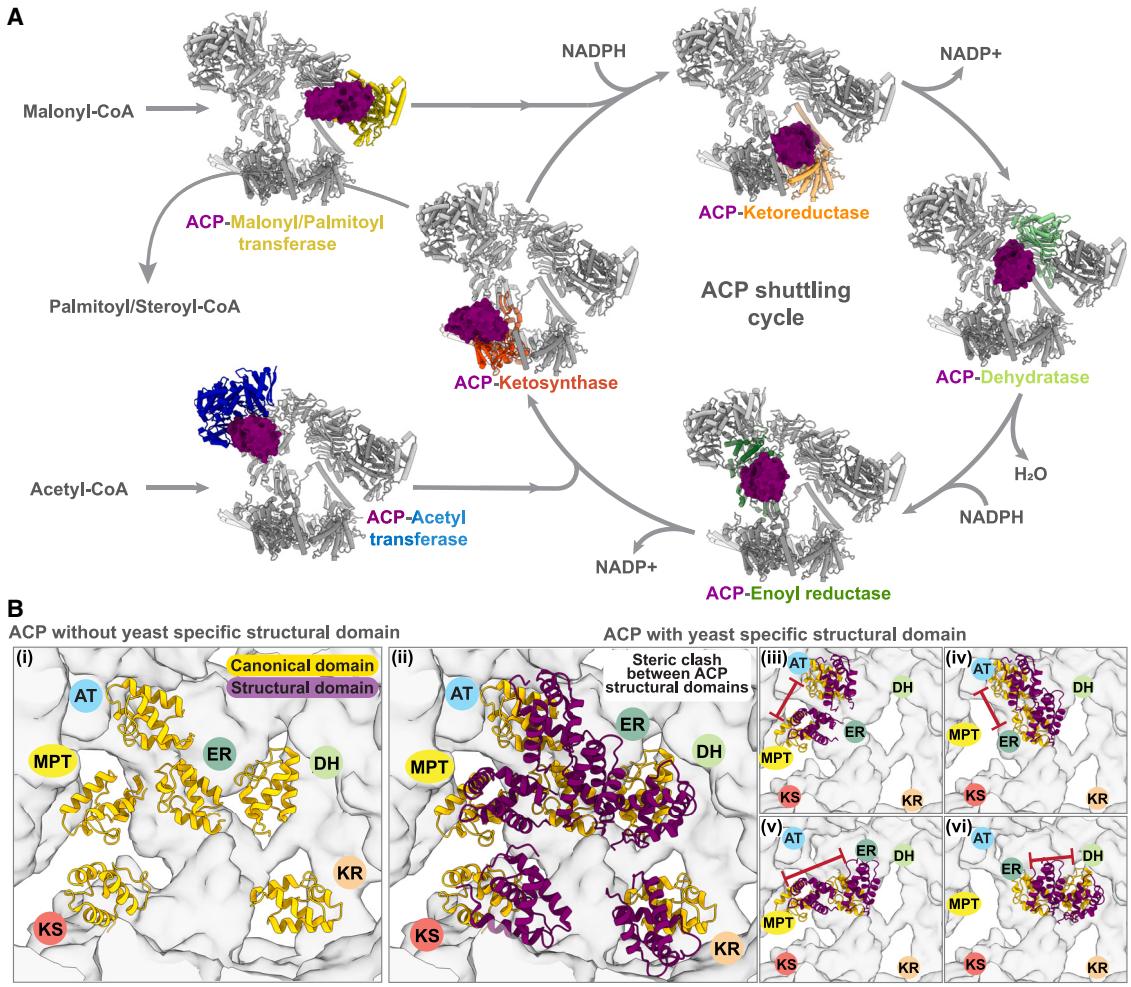

Figure 7. Structural snapshots of ACP domains in the FA biosynthesis cycle

(A) Architectural framework of the yeast FA biosynthesis cycle. Shown are asymmetric units of yFAS (gray ribbon diagram) and ACP domains (violet) occupying distinct positions, representing intermediates in the FA biosynthesis cycle. In these distinct positions, the domain to which ACP is bound is colored: AT (blue), MPT (yellow), KS (red), KR (orange), DH (light green), and ER (dark green). All states were resolved in this manuscript, with the exception of the previously reported[12] DH-bound state.

(B) Comparison of ACP domain binding to enzymatic domains in the absence (i) and presence (ii) of the yeast-specific structural ACP domain. When bound to AT (iii and iv), MPT (iii and v), ER (iv–vi), and DH domains (vi), the structural domain exerts a steric hindrance to ACP binding to the adjacent enzymatic domain. In the absence of the ACP structural domain, such binding is unimpeded. A "path of least resistance" is thus established that delineates a "functional compartment" where active sites are arranged as depicted in (ii).

Related to Figure S7.

better than 2.2 Å. Particularly in cryo-EM, many factors represent impediments to attaining such detailed structures: biochemical, compositional, and conformational heterogeneities; heterogeneity arising from cryo-EM grid preparation; technical EM imaging limitations; and pitfalls arising from low signal-to-noise image processing.

For *S. cerevisiae* FAS, we have tackled biochemical heterogeneity by establishing a mild chromatography-free purification procedure that allows FAS structure determination by cryo-EM and X-ray crystallography to be better than 3 Å.[11] We discovered a weakly bound γ subunit of yFAS that readily dissociates in the concentrations used for cryo-EM grid preparation. To overcome this, we purified FAS from an *S. cerevisiae* strain with a genetic deletion for the γ subunit. We additionally added saturating concentrations of malonyl-CoA and $NADP^+$ to lock the respective enzymatic domains in uniform compositional states. For cryo-EM structure determination, we used a 300 kV Titan Krios Mono/BCOR microscope with optimized electron optics.[14] In the case of yFAS, this has led to structure determination at a global resolution of 1.9 Å, an experimental B-factor of 53 $Å^2$, and a local resolution spread from 1.9 Å at the central wheel to 2.7 Å at the top of the dome (Figures 1B–1D and S1). The B-factor obtained for yFAS with the 300 kV Titan Krios Mono/BCOR microscope is similar to apo-ferritin imaged with a conventional Titan G3 Krios instrument.[28] This highlights that EM optical improvements aid in improving the resolution attained by

almost 1 Å proportional to the previously described local resolution spread, even for dynamic assemblies such as FAS.[11,15] The high-resolution structure has confirmed that FMN is present in its reduced form in the ER (Figures 1Di and S1H), provided insights into CoA recognition and a covalent Ser1808-malonyl adduct in the MPT (Figure 1Dv), and NADPH/NADP$^+$ recognition by protein and ordered solvent in the KR and ER (Figures 1Dii–1Div and S1I). However, notably, the ACP domain is not resolved in the high-resolution structure (Figure 1) and is partially visible in numbers exceeding those dictated by its biochemical composition in other instances (Figure 2). This can either be explained by (1) insufficient biochemical control to synchronize in distinct functional states and/or (2) an orientation assignment problem in image alignments due to the pseudo-symmetric dome, resulting in difficulties to sort for conformational heterogeneity, independent- and asynchronous ACP motions, and failure to detect ACPs in whole FAS particles.

Structural ACP snapshots and conformational states in the FA synthesis cycle

Standard 3D classification procedures were unable to reveal ACP domains in full FAS. Sorting for ACP positions and β subunit conformations by computationally extracting FAS asymmetric units has visualized ACP snapshots representing functional intermediates in the FA synthesis cycle. Two additional hybrid β subunit conformations representing transitions from rotated to non-rotated conformations were identified (Figure 3A). An inventory of β subunit conformations and corresponding ACP positions suggests that the rotated state is exclusively reserved for the AT-bound ACP position (Figure 5A). The AT-bound ACP is also compatible with SRot, SNRot, and non-rotated conformations (Figures 3B and 5A; Video S2). We thus infer that catalytic AT serine loading by the starter acetyl group is followed by ACP movement to the AT domain and Ppant-arm positioning to accept the acetyl group. ACP-AT binding is most likely accompanied by a non-rotated to rotated state conformational change. When transferring the acetyl group to the KS catalytic cysteine, ACP domain motion to the KS and non-rotated state adoption must occur. These changes and ACP motions are sufficient to explain the energy barrier we had previously reported[11] in the transition from rotated to non-rotated conformations. We had previously speculated[11] that every FAS functional state would adopt a distinct β subunit conformation. The β subunit conformation/ACP location survey in Figure 5A does not confirm this. ACP binding to every other enzymatic domain occurs in the non-rotated conformation. This might avoid kinetic barriers in condensation and elongation cycles and increase processivity.

Small-scale conformational changes very much do occur in condensation and elongation cycles. For FA biosynthesis, the malonyl group must be activated by the MPT catalytic serine and transferred onto the ACP Ppant arm (Figures 1Dv, 3Ci, 3Cii, and 4A). MPT closes when malonyl-CoA is bound, opens to release CoA, and closes again to accommodate the ACP-Ppant arm to enable malonyl transfer. The ACP-bound MPT active site is more spacious, allowing larger ACP-bound acyl chain accommodation for release; however, how palmitoyl- or stearoyl-Ppant-acyl adducts might bind remains unclear at present. The malonyl-Ppant adduct is then taken to the KS, where a Claisen condensation reaction forms a β-keto intermediate. NADPH then populates the KR active site, causing KR loop clamping onto NADPH (Figures 1A and 4C), expanding the space for Ppant-arm entry and accommodating β-keto intermediates (Figures 4C and 4D). Following reduction to a β-hydroxy intermediate, the ACP proceeds to the DH[12] to form a *trans*-2-enoyl intermediate. Dehydration most likely establishes the *cis*- or *trans*-configuration of the enoyl intermediate and the following regiospecificity. However, neither does the published structure[12] resolve the Ppant arm nor were we yet able to observe this state in our own experiments to address this question. To complete the FA biosynthesis cycle (Figure 1A), the ACP interacts with reduced FMN in the ER where the Ppant-arm kinks, and its binding leads to the constriction of the NADPH/NADP$^+$ binding cleft (Figure 4E). ACP Ppant-enoyl adduct and NADPH/NADP$^+$ binding are mutually exclusive, suggesting either NADPH/NADP$^+$ departure before ACP arrival or that ACP binding triggers NADPH/NADP$^+$ release. The ACP then transfers the Ppant-fatty acyl adduct to either the KS active site cysteine for additional elongation cycles or the MPT domain, where the Ppant-acyl adduct is *trans*-acetylated to a CoA molecule and released. Associated with the multiple steps in which the ACP is KS-bound (transfer of acetyl, condensation of acetyl with malonyl, and condensation and transfer of various fatty acyl-lengths with malonyl), the biochemical heterogeneity appears to be too large to resolve the Ppant arm. However, we were able to resolve the Ppant arm both by cryo-EM and X-ray crystallography when using cycled FAS as previously reported.[11] We thus hypothesize that KS Ppant-recognition might be significantly different depending on the precise nature of the acyl adduct carried by the ACP domain. A series of structures at high resolution with defined intermediates bound to the catalytic cysteine of the KS will be essential to resolve this matter.

Larger ACP in fungal type I FAS appears to bring order within the FAS dome

A possible logistical problem imposed by the spatial confines of yFAS architecture looms: the common use of ACP domain and its Ppant arm could elicit promiscuity in recognition. Bacterial FAS enzyme-ACP interactions rely on a minimal interaction interface that encompasses the Ppant arm and electrostatic interactions (Figures S5 and S6).[1,6,23,24] Promiscuous ACP binding to sites in a different order than the one strictly required by the FA biosynthetic sequence would decrease catalytic efficiency. A potential resolution of this problem could be the additional structural domain of yFAS.[1,5] Indeed, we observe the association between yACP structural domains and the structural domains of several enzymatic domains (Figures S5 and S6). Taking all the data summarized in Figure 7A into account, we are able to conclude that the canonical yACP domain extensively contacts all active sites and is often supplemented by interactions with the structural domain. yFAS-yACP interaction affinity, as studied by BSAs in interfaces, appears to be conserved in comparison to bacterial counterparts but pronouncedly distributed between yACP canonical domain-active site cleft interactions and yACP structural domain-structural segment interactions (Figures S5 and S6). Thus, ACP recognition is likely to be governed by avidity rather than affinity in type I FAS. In addition, the mode of yACP

positioning at enzymatic domains suggests that the yACP structural domain may play a more active role. yACP binding by steric hindrance is mutually exclusive between (1) AT and its proximal MPT and ER domains, (2) MPT and its proximal AT and ER domains, and (3) DH and its proximal ER domain (Figures 7Bii–7Bvi). The steric hindrance would be less pronounced in the absence of the yACP structural domain (Figure 7Bi). Notably, the "path of least resistance" for the ACP to shuttle along the FA biosynthetic sequence is common to the functional compartment we inferred by γ subunit binding.[11] Thus, the shuttling path least obstructed by the yACP structural domain coincides with the shortest path required to traverse the FAS dome, ultimately increasing FA biosynthetic productivity. Another consequence of the yACP structural domain-exerted steric hindrance is ensuring that the enzyme-active site to which the ACP next transitions is empty. Therefore, in addition to minimizing recognition promiscuity, the yACP structural domain may promote compartmentalization and ensure productive sequential order in FA biosynthesis.

Limitations of the study

Despite advancing our understanding of the yeast FA biosynthesis cycle, the present study also illustrates some technical challenges that remain to be addressed. By disentangling individual functional compartments, we have been able to resolve structural snapshots of FA biosynthesis intermediates. However, this precisely impedes gaining any insights into possible allosteric regulatory mechanisms that might be at play within the whole particle. The inability to directly sort individual ACP states within the whole FAS highlights the need for further technical improvements in EMs and image processing algorithms. The apparent asynchrony in ACP movement raises the necessity for further biochemical control in the precise trapping of intermediates, for which the findings reported here will provide essential structural insights. Mechanism-based crosslinking using CoA derivatives[29] appears predestined for this purpose. Irrespective of the exact nature, precisely advanced biochemical trapping will be essential to attain structures at higher resolution by both cryo-EM and X-ray crystallography. Finally, the structural framework provided here elucidates a proof-of-concept for the biotechnological exploitation of fungal type I FAS that is to be expanded in the future.

STAR★METHODS

Detailed methods are provided in the online version of this paper and include the following:

- KEY RESOURCES TABLE
- RESOURCE AVAILABILITY
  - Lead contact
  - Materials availability
  - Data and code availability
- EXPERIMENTAL MODEL AND STUDY PARTICIPANT DETAILS
  - Yeast culture
  - Bacterial culture
- METHOD DETAILS
  - Purification of yeast FAS
  - Purification of recombinant proteins
  - Cryo-EM sample preparation
  - Cryo-EM grid preparation
  - Cryo-EM data collection and image processing
  - Cryo-EM Model building
  - Enzyme assays and semiquantitative analysis of CoA derivatives
  - Sequence conservation analysis
- QUANTIFICATION AND STATISTICAL ANALYSIS
  - Calculating ACP distribution per asymmetric unit
  - Semiquantitative analysis of CoA derivates

SUPPLEMENTAL INFORMATION

Supplemental information can be found online at https://doi.org/10.1016/j.cell.2023.10.009.

ACKNOWLEDGMENTS

We thank Thomas Schultz for help with yeast fermentation and Gabi Heyne, Suzan van Gerwen, and Gesa Martens for technical assistance. This work was funded by the Max-Planck Society and the Deutsche Forschungsgemeinschaft (CRC 1456/A05).

AUTHOR CONTRIBUTIONS

A.C. and H.S. conceived the work and supervised all research; K.S. performed the structural work; G.B. analyzed and calculated ACP distributions; B.G. reconstituted samples, performed assays for LC/MS, and analyzed LC/MS data; K.M.Y. assisted in high-resolution EM data collection and processing; M.N.-S. acquired LC/MS data and analyzed them; A.C. wrote the manuscript; and all authors reviewed the data and the manuscript.

DECLARATION OF INTERESTS

A.C. and H.S. have filed a patent for the purification procedure described herein (EP16/17/3037, USSN 62/345,913). A.C., H.S., K.S., and B.G. have filed a patent for the exploitation of the γ subunit (EP19/16/3958). A.C., H.S., and K.S. have filed a patent for the exploitation of the structural snapshots reported in this manuscript.

Received: July 28, 2021
Revised: July 21, 2023
Accepted: October 5, 2023
Published: November 9, 2023

REFERENCES

1. Chan, D.I., and Vogel, H.J. (2010). Current understanding of fatty acid biosynthesis and the acyl carrier protein. Biochem. J. *430*, 1–19. https://doi.org/10.1042/BJ20100462.
2. Lynen, F. (1980). On the structure of fatty acid synthetase of yeast. Eur. J. Biochem. *112*, 431–442. https://doi.org/10.1111/j.1432-1033.1980.tb06105.x.
3. White, S.W., Zheng, J., Zhang, Y.M., and Rock, C.O. (2005). The structural biology of TYPE II fatty acid biosynthesis. Annu. Rev. Biochem. *74*, 791–831. https://doi.org/10.1146/annurev.biochem.74.082803.133524.
4. Schweizer, E., and Hofmann, J. (2004). Microbial type I fatty acid synthases (FAS): major players in a network of cellular FAS systems. Microbiol. Mol. Biol. Rev. *68*, 501–517. https://doi.org/10.1128/MMBR.68.3.501-517.2004.
5. Günenc, A.N., Graf, B., Stark, H., and Chari, A. (2022). Fatty acid synthase: structure, function, and regulation. In Sub-Cellular Biochemistry, J.R.

Harris and J. Marles-Wright, eds. (Springer International Publishing), pp. 1–33. https://doi.org/10.1007/978-3-031-00793-4_1.

6. Nguyen, C., Haushalter, R.W., Lee, D.J., Markwick, P.R.L., Bruegger, J., Caldara-Festin, G., Finzel, K., Jackson, D.R., Ishikawa, F., O'Dowd, B., et al. (2014). Trapping the dynamic acyl carrier protein in fatty acid biosynthesis. Nature *505*, 427–431. https://doi.org/10.1038/nature12810.

7. Perez, D.R., Leibundgut, M., and Wider, G. (2015). Interactions of the acyl chain with the Saccharomyces cerevisiae acyl carrier protein. Biochemistry *54*, 2205–2213. https://doi.org/10.1021/bi5014563.

8. Garima, Prem, R., Yadav, U., and Sundd, M. (2021). A GX2GX3G motif facilitates acyl chain sequestration by Saccharomyces cerevisiae acyl carrier protein. J. Biol. Chem. *297*, 101394. https://doi.org/10.1016/j.jbc.2021.101394.

9. Leibundgut, M., Jenni, S., Frick, C., and Ban, N. (2007). Structural basis for substrate delivery by acyl carrier protein in the yeast fatty acid synthase. Science *316*, 288–290. https://doi.org/10.1126/science.1138249.

10. Lomakin, I.B., Xiong, Y., and Steitz, T.A. (2007). The crystal structure of yeast fatty acid synthase, a cellular machine with eight active sites working together. Cell *129*, 319–332. https://doi.org/10.1016/j.cell.2007.03.013.

11. Singh, K., Graf, B., Linden, A., Sautner, V., Urlaub, H., Tittmann, K., Stark, H., and Chari, A. (2020). Discovery of a regulatory subunit of the yeast fatty acid synthase. Cell *180*, 1130–1143.e20. https://doi.org/10.1016/j.cell.2020.02.034.

12. Lou, J.W., and Mazhab-Jafari, M.T. (2020). Steric occlusion regulates proximal interactions of acyl carrier protein domain in fungal fatty acid synthase. Commun. Biol. *3*, 274. https://doi.org/10.1038/s42003-020-0997-y.

13. Anselmi, C., Grininger, M., Gipson, P., and Faraldo-Gómez, J.D. (2010). Mechanism of substrate shuttling by the acyl-carrier protein within the fatty acid mega-synthase. J. Am. Chem. Soc. *132*, 12357–12364. https://doi.org/10.1021/ja103354w.

14. Yip, K.M., Fischer, N., Paknia, E., Chari, A., and Stark, H. (2020). Atomic-resolution protein structure determination by cryo-EM. Nature *587*, 157–161. https://doi.org/10.1038/s41586-020-2833-4.

15. Joppe, M., D'Imprima, E., Salustros, N., Paithankar, K.S., Vonck, J., Grininger, M., and Kühlbrandt, W. (2020). The resolution revolution in cryoEM requires high-quality sample preparation: a rapid pipeline to a high-resolution map of yeast fatty acid synthase. IUCrJ *7*, 220–227. https://doi.org/10.1107/S2052252519017366.

16. Elad, N., Baron, S., Peleg, Y., Albeck, S., Grunwald, J., Raviv, G., Shakked, Z., Zimhony, O., and Diskin, R. (2018). Structure of type-I Mycobacterium tuberculosis fatty acid synthase at 3.3 Å resolution. Nat. Commun. *9*, 3886. https://doi.org/10.1038/s41467-018-06440-6.

17. Lou, J.W., Iyer, K.R., Hasan, S.M.N., Cowen, L.E., and Mazhab-Jafari, M.T. (2019). Electron cryomicroscopy observation of acyl carrier protein translocation in type I fungal fatty acid synthase. Sci. Rep. *9*, 12987. https://doi.org/10.1038/s41598-019-49261-3.

18. Snowden, J.S., Alzahrani, J., Sherry, L., Stacey, M., Rowlands, D.J., Ranson, N.A., and Stonehouse, N.J. (2021). Structural insight into pichia pastoris fatty acid synthase. Sci. Rep. *11*, 9773. https://doi.org/10.1038/s41598-021-89196-2.

19. Huiskonen, J.T. (2018). Image processing for cryogenic transmission electron microscopy of symmetry-mismatched complexes. Biosci. Rep. *38*, 1–13. https://doi.org/10.1042/BSR20170203.

20. Scheres, S.H.W. (2016). Processing of Structurally Heterogeneous Cryo-EM Data in RELION, First Edition (Elsevier Inc.). https://doi.org/10.1016/bs.mie.2016.04.012.

21. Gipson, P., Mills, D.J., Wouts, R., Grininger, M., Vonck, J., and Kühlbrandt, W. (2010). Direct structural insight into the substrate-shuttling mechanism of yeast fatty acid synthase by electron cryomicroscopy. Proc. Natl. Acad. Sci. USA *107*, 9164–9169. https://doi.org/10.1073/pnas.0913547107.

22. Jenni, S., Leibundgut, M., Boehringer, D., Frick, C., Mikolásek, B., and Ban, N. (2007). Structure of fungal fatty acid synthase and implications for iterative substrate shuttling. Science *316*, 254–261. https://doi.org/10.1126/science.1138248.

23. Misson, L.E., Mindrebo, J.T., Davis, T.D., Patel, A., McCammon, J.A., Noel, J.P., and Burkart, M.D. (2020). Interfacial plasticity facilitates high reaction rate of E. coli FAS malonyl-CoA:ACP transacylase, FabD. Proc. Natl. Acad. Sci. USA *117*, 24224–24233. https://doi.org/10.1073/pnas.2009805117.

24. Mindrebo, J.T., Patel, A., Kim, W.E., Davis, T.D., Chen, A., Bartholow, T.G., La Clair, J.J., McCammon, J.A., Noel, J.P., and Burkart, M.D. (2020). Gating mechanism of elongating β-ketoacyl-ACP synthases. Nat. Commun. *11*, 1727. https://doi.org/10.1038/s41467-020-15455-x.

25. Hevener, K.E., Santarsiero, B.D., Lee, H., Jones, J.A., Boci, T., Johnson, M.E., and Mehboob, S. (2018). Structural characterization of Porphyromonas gingivalis enoyl-ACP reductase II (FabK). Acta Crystallogr. F Struct. Biol. Commun. *74*, 105–112. https://doi.org/10.1107/S2053230X18000262.

26. Price, A.C., Zhang, Y.M., Rock, C.O., and White, S.W. (2004). Cofactor-induced conformational rearrangements establish a catalytically competent active site and a proton relay conduit in FabG. Structure *12*, 417–428. https://doi.org/10.1016/J.STR.2004.02.008.

27. Roh, S.H., Hryc, C.F., Jeong, H.H., Fei, X., Jakana, J., Lorimer, G.H., and Chiu, W. (2017). Subunit conformational variation within individual GroEL oligomers resolved by Cryo-EM. Proc. Natl. Acad. Sci. USA *114*, 8259–8264. https://doi.org/10.1073/pnas.1704725114.

28. Danev, R., Yanagisawa, H., and Kikkawa, M. (2019). Cryo-electron microscopy methodology: current aspects and future directions. Trends Biochem. Sci. *44*, 837–848. https://doi.org/10.1016/j.tibs.2019.04.008.

29. Finzel, K., Lee, D.J., and Burkart, M.D. (2015). Using modern tools to probe the structure-function relationship of fatty acid synthases. Chembiochem *16*, 528–547. https://doi.org/10.1002/cbic.201402578.

30. Winn, M.D., Ballard, C.C., Cowtan, K.D., Dodson, E.J., Emsley, P., Evans, P.R., Keegan, R.M., Krissinel, E.B., Leslie, A.G.W., McCoy, A., et al. (2011). Overview of the CCP4 suite and current developments. Acta Crystallogr. D Biol. Crystallogr. *67*, 235–242. https://doi.org/10.1107/S0907444910045749.

31. Madeira, F., Pearce, M., Tivey, A.R.N., Basutkar, P., Lee, J., Edbali, O., Madhusoodanan, N., Kolesnikov, A., and Lopez, R. (2022). Search and sequence analysis tools services from EMBL-EBI in 2022. Nucleic Acids Res. *50*, W276–W279. https://doi.org/10.1093/nar/gkac240.

32. Rohou, A., and Grigorieff, N. (2015). CTFFIND4: fast and accurate defocus estimation from electron micrographs. J. Struct. Biol. *192*, 216–221. https://doi.org/10.1016/j.jsb.2015.08.008.

33. Emsley, P., and Cowtan, K. (2004). *Coot*: model-building tools for molecular graphics. Acta Crystallogr. D Biol. Crystallogr. *60*, 2126–2132. https://doi.org/10.1107/S0907444904019158.

34. Lebedev, A.A., Young, P., Isupov, M.N., Moroz, O.V., Vagin, A.A., and Murshudov, G.N. (2012). JLigand: a graphical tool for the CCP4 template-restraint library. Acta Crystallogr. D Biol. Crystallogr. *68*, 431–440. https://doi.org/10.1107/S090744491200251X.

35. Adams, P.D., Afonine, P.V., Bunkóczi, G., Chen, V.B., Davis, I.W., Echols, N., Headd, J.J., Hung, L.W., Kapral, G.J., Grosse-Kunstleve, R.W., et al. (2010). *PHENIX*: a comprehensive Python-based system for macromolecular structure solution. Acta Crystallogr. D Biol. Crystallogr. *66*, 213–221. https://doi.org/10.1107/S0907444909052925.

36. Schrödinger, LLC (2015). The PyMOL molecular graphics system. Version 1.8 (PyMOL. https://pymol.org/2/.

37. Murshudov, G.N., Skubák, P., Lebedev, A.A., Pannu, N.S., Steiner, R.A., Nicholls, R.A., Winn, M.D., Long, F., and Vagin, A.A. (2011). REFMAC5 for the refinement of macromolecular crystal structures. Acta Crystallogr. D Biol. Crystallogr. *67*, 355–367. https://doi.org/10.1107/S0907444911001314.

38. Zivanov, J., Nakane, T., and Scheres, S.H.W. (2020). Estimation of high-order aberrations and anisotropic magnification from cryo-EM

data sets in RELION-3.1. IUCrJ *7*, 253–267. https://doi.org/10.1107/S2052252520000081.

39. Pettersen, E.F., Goddard, T.D., Huang, C.C., Couch, G.S., Greenblatt, D.M., Meng, E.C., and Ferrin, T.E. (2004). UCSF Chimera—a visualization system for exploratory research and analysis. J. Comput. Chem. *25*, 1605–1612. https://doi.org/10.1002/jcc.20084.

40. Goddard, T.D., Huang, C.C., Meng, E.C., Pettersen, E.F., Couch, G.S., Morris, J.H., and Ferrin, T.E. (2018). UCSF ChimeraX: meeting modern challenges in visualization and analysis. Protein Sci. *27*, 14–25. https://doi.org/10.1002/pro.3235.

41. Zheng, S.Q., Palovcak, E., Armache, J.P., Verba, K.A., Cheng, Y., and Agard, D.A. (2017). MotionCor2: anisotropic correction of beam-induced motion for improved cryo-electron microscopy. Nat. Methods *14*, 331–332. https://doi.org/10.1038/nmeth.4193.

42. Zivanov, J., Nakane, T., Forsberg, B.O., Kimanius, D., Hagen, W.J., Lindahl, E., and Scheres, S.H. (2018). New tools for automated high-resolution cryo-EM structure determination in RELION-3. eLife *7*. https://doi.org/10.7554/eLife.42166.

43. Russo, C.J., and Henderson, R. (2018). Ewald sphere correction using a single side-band image processing algorithm. Ultramicroscopy *187*, 26–33. https://doi.org/10.1016/J.ULTRAMIC.2017.11.001.

44. Wolf, J., Stark, H., Fafenrot, K., Albersmeier, A., Pham, T.K., Müller, K.B., Meyer, B.H., Hoffmann, L., Shen, L., Albaum, S.P., et al. (2016). A systems biology approach reveals major metabolic changes in the thermoacidophilic archaeon Sulfolobus solfataricus in response to the carbon source L-fucose versus D-glucose. Mol. Microbiol. *102*, 882–908. https://doi.org/10.1111/mmi.13498.

45. Reback, C.J., McKinney, W., Kisler, K.A., jbrockmendel, Van den Bossche, J., Augspurger, T., Cloud, P., gfyoung; Sinhrks, Klein, A., Roeschke, M., et al. (2020). pandas-dev/pandas: Pandas 1.0.3. https://doi.org/10.5281/ZENODO.3715232.

STAR★METHODS

KEY RESOURCES TABLE

REAGENT or RESOURCE	SOURCE	IDENTIFIER
Bacterial and virus strains		
E. coli BL21 Star	ThermoFisher Scientific	Cat#C601003
E. coli BL21-AI	ThermoFisher Scientific	Cat#C607003
Chemicals, peptides, and recombinant proteins		
Nicotinamide adenine dinucleotide phosphate ($NADP^+$)	Roth	Cat#AE13.1
Nicotinamide adenine dinucleotide phosphate (NADPH)	Roth	Cat#AE14.1
Bovine serum albumin	Sigma-Aldrich	Cat#A7030
Malonyl-CoA	Sigma-Aldrich	Cat#M4263
Acetyl-CoA	Sigma-Aldrich	Cat#A2181
04:0 Coenzyme A	Sigma-Aldrich	Cat#870704P
06:0 Coenzyme A	Sigma-Aldrich	Cat#870706P
08:0 Coenzyme A	Sigma-Aldrich	Cat#870708P
10:0 Coenzyme A	Sigma-Aldrich	Cat#870710P
12:0 Coenzyme A	Sigma-Aldrich	Cat#870712P
14:0 Coenzyme A	Sigma-Aldrich	Cat#870714P
16:0 Coenzyme A	Sigma-Aldrich	Cat#870716P
18:0 Coenzyme A	Sigma-Aldrich	Cat#870718P
Benzamidine chloride	Sigma-Aldrich	Cat#B6506
Octyl glucose neopentyl glycol (OGNG)	Anatrace	Cat#NG311
Lauryl maltose neopentyl glycol (LMNG)	Anatrace	Cat#NG310
PolyEthyleneGlycol400	Sigma-Aldrich	Cat#81172
DTT	Roth	Cat#6908.2
TCEP	UBPbio	Cat#P1020
Bradford dye reagent	Biorad	Cat#5000205
γ-subunit	Singh et al.[11]	N/A
γ-1xUnaG	This paper	N/A
γ-2xUnaG	This paper	N/A
γ-Tes	This paper	N/A
Tes	This paper	N/A
Deposited data		
Crystallographic structure of Δγ-FAS complex	Singh et al.[11]	PDB: 6QL9
Δγ-FAS at 1.9Å resolution	This paper	PDB: 8PRW, EMDB: EMD-17840
FAS asymmetric unit with non-rotated conformation and ACP at KR domain in the FASamn sample (acetyl-CoA, malonyl-CoA, and $NADP^+$)	This paper	PDB: 8PRV, EMDB: EMD-17839
FAS asymmetric unit with non-rotated conformation and ACP at KS domain in the FASamn sample (acetyl-CoA, malonyl-CoA, and $NADP^+$)	This paper	PDB: 8PS1, EMDB: EMD-17842
FAS asymmetric unit with non-rotated conformation and ACP at ER domain in the FASam sample (acetyl-CoA and malonyl-CoA)	This paper	PDB: 8PS2, EMDB: EMD-17843
FAS asymmetric unit with non-rotated conformation and ACP at KS domain in the FASam sample (acetyl-CoA and malonyl-CoA)	This paper	PDB: 8PS9, EMDB: EMD-17847
FAS asymmetric unit with semi non-rotated conformation and ACP at ER domain in the FASam sample (acetyl-CoA and malonyl-CoA)	This paper	PDB: 8PS8, EMDB: EMD-17846

(*Continued on next page*)

Continued

REAGENT or RESOURCE	SOURCE	IDENTIFIER
FAS asymmetric unit with semi non-rotated conformation and ACP at KS domain in the FASam sample (acetyl-CoA, and malonyl-CoA)	This paper	PDB: 8PSA, EMDB: EMD-17848
FAS asymmetric unit with rotated conformation and ACP at AT domain in the FASx sample (absence of substrates)	This paper	PDB: 8PSP, EMDB: EMD-17859
FAS asymmetric unit with semi rotated conformation and ACP at AT domain in the FASx sample (absence of substrates)	This paper	PDB: 8PSJ, EMDB: EMD-17853
FAS asymmetric unit with semi non-rotated conformation and ACP at AT domain in the FASx sample (absence of substrates)	This paper	PDB: 8PSG, EMDB: EMD-17852
FAS asymmetric unit with non-rotated conformation and ACP at AT domain in the FASx sample (absence of substrates)	This paper	PDB: 8PSF, EMDB: EMD-17851
FAS asymmetric unit with non-rotated conformation and ACP at KS domain in the FASx sample (absence of substrates)	This paper	PDB: 8PSK, EMDB: EMD-17854
FAS asymmetric unit with semi non-rotated conformation and ACP at KS domain in the FASx sample (absence of substrates)	This paper	PDB: 8PSL, EMDB: EMD-17855
FAS asymmetric unit with non-rotated conformation and ACP at MPT domain in the FASx sample (absence of substrates)	This paper	PDB: 8PSM, EMDB: EMD-17856
Experimental models: Organisms/strains		
S. cerevisiae tma17Δ BJ2168 (MATa prc1-407 prb1-1122 pep4-3 leu2 trp1 ura3-52 gal2 ydl110c::kanMX)	Singh et al.[11]	N/A
Recombinant DNA		
γ-pET151/D-TOPO	Singh et al.[11]	N/A
γ-1xUnaG-pET151/D-TOPO	This paper	N/A
γ-2xUnaG-pET151/D-TOPO	This paper	N/A
γ-Tes-pET151/D-TOPO	This paper	N/A
Tes-pET151/D-TOPO	This paper	N/A
Software and algorithms		
CCP4	Winn et al.[30]	http://www.ccp4.ac.uk
Clustal Omega	Clustal Omega[31]	https://www.ebi.ac.uk/Tools/msa/clustalo/
CTFFIND 4.1.14	Rohou and Grigorieff[32]	https://grigoriefflab.umassmed.edu/ctffind4
Coot v.0.8.9	Emsley and Cowtan[33]	https://www2.mrclmb.cam.ac.uk/personal/pemsley/coot
Gautomatch	Dr. Kai Zhang	http://www.mrc-lmb.cam.ac.uk/kzhang
JLigand	Lebedev et al.[34]	http://www.ysbl.york.ac.uk/mxstat/JLigand
Phenix	Adams et al.[35]	https://www.phenix-online.org/
PyMOL	Schrödinger, LLC[36]	https://www.pymol.org
Refmac5	Murshudov et al.[37]	https://www2.mrc-lmb.cam.ac.uk/groups/murshudov/content/refmac/refmac.html
RELION 3.1	Zivanov et al.[38]	http://www2.mrc-lmb.cam.ac.uk/relion
UCSF Chimera	Pettersen et al.[39]	http://www.cgl.ucsf.edu/chimera
UCSF Chimera X	Goddard et al.[40]	https://www.cgl.ucsf.edu/chimerax/
Other		
UltrAuFoil R1.5/1.6, 300-mesh grids	Quantifoil	N/A
Quantifoil R3.5/1 (Cu), 200 Mesh grids	Quantifoil	N/A
Quantifoil R2/2 (Cu), 200 Mesh grids	Quantifoil	N/A

RESOURCE AVAILABILITY

Lead contact

Further information and requests for resources and reagents should be directed to the Lead Contact: Ashwin Chari (ashwin.chari@mpibpc.mpg.de).

Materials availability

All unique/stable reagents and plasmids generated in this study are available from the lead contact with a completed material transfer agreement.

Data and code availability

- The coordinates for the determined structures are deposited in the Protein Data Bank (PDB) accession codes: PDB: 8PRV, PDB: 8PRW, PDB: 8PS1, PDB: 8PS2, PDB: 8PS8, PDB: 8PS9, PDB: 8PSA, PDB: 8PSF, PDB: 8PSG, PDB: 8PSJ, PDB: 8PSK, PDB: 8PSL, PDB: 8PSM, and PDB: 8PSP. EM maps are deposited with the (EMDB) accession codes: EMDB: EMD-17839, EMDB: EMD-17840, EMDB: EMD-17842, EMDB: EMD-17843, EMDB: EMD-17846, EMDB: EMD-17847, EMDB: EMD-17848, EMDB: EMD-17851, EMDB: EMD-17852, EMDB: EMD-17853, EMDB: EMD-17854, EMDB: EMD-17855, EMDB: EMD-17856, and EMDB: EMD-17859.
- This paper does not report original code.
- Any additional information required to reanalyze the data reported in this paper is available from the lead contact upon request.

EXPERIMENTAL MODEL AND STUDY PARTICIPANT DETAILS

Yeast culture

Saccharomyces cerevisiae strain tma17Δ BJ2168 (MATa prc1-407 prb1-1122 pep4-3 leu2 trp1 ura3-52 gal2 tma17::kanMX)[11] was used in this study. Cells were grown in YPD medium in an Infors 250 litre fermenter and harvested in late log phase at an OD_{600} of 9-10. Subsequently, cells were washed with cold ddH_2O and resuspended in 2X purification buffer (0.05 M BisTris pH 6.5, 0.05 M potassium acetate, 0.01 M magnesium acetate) containing 20% (w/v) sucrose such that 2 mL of buffer was added per gram of cells. Cells were then flash frozen as beads in liquid nitrogen and stored at -80°C until further use.

Bacterial culture

For expression of γ-1xUnaG, γ-2xUnaG, γ-Tes, or Tes the respective plasmids were transformed into chemically competent BL21-AI (ThermoFisher Scientific; γ-Tes or Tes) or BL21 Star (ThermoFisher Scientific; γ-1xUnaG or γ-2xUnaG) cells. Starting cultures were grown in LB with 1% (w/v) glucose over night at 37°C. 500 mL cultures in TB medium inoculated using the pre- culture to an OD600 of 0.05 were grown with 1% glucose (w/v) and antibiotics. Cultures were grown (37°C, 180 rpm) until an OD600 of 0.6-0.8 was reached, the temperature lowered to 18°C, and after 1 hour incubation cultures were induced by addition of 1 mM IPTG (BL21 Star cultures), or 1 mM IPTG and 2% (w/v) L-arabinose (BL21-AI cultures). Overexpression was performed for 16 hours at 18°C. Cells were harvested by centrifugation (5,000 g, 5 min, 4°C), resuspended and washed with ice-cold 1x PBS-buffer (137 mM NaCl, 2.7 mM KCl, 10 mM Na2HPO4, 1.8 mM KH2PO4; pH 7.4), and centrifuged again (5000 g, 5 min, 4°C). The final pellet was flash frozen in liquid nitrogen and stored at -80°C.

METHOD DETAILS

Purification of yeast FAS

FAS was purified as described by Singh et al.[11] We started with 700 g of frozen cell beads (corresponding to 233 g wet cell weight of yeast), which were ground in liquid nitrogen to a fine powder using a Retsch ZM200 mill. The ground powder was thawed in a water bath at 37°C, supplemented with purification buffer (0.05 M BisTris pH 6.5, 0.05 M potassium acetate, 0.01 M magnesium acetate) to 0.33X concentration from a 10X stock, followed by the addition of sucrose powder to 20% (w/v), benzamidine chloride to 10 mM and PMSF to 1 mM (from a 100 mM stock solution in propanol). The extract was incubated at 25°C on a magnetic stirrer for 30 minutes followed by centrifugation at 30,000 rcf for 30 minutes at 4°C. After centrifugation, the supernatant was filtered through 3 layers each of cheese cloth and miracloth to obtain a S30 yeast cell extract. To this, Octyl Glucose Neopentyl Glycol (OGNG) (from a 10% (w/v) stock) was added to a final concentration of 0.2% (v/v) and the extract was incubated at 30°C for 30 minutes followed by centrifugation at 100,000 rcf for 1 hour at 4°C. The supernatant was again filtered through 3 layers each of cheese cloth and miracloth. The thus clarified S100 extract was subjected to differential precipitation with PolyEthyleneGlycol400 (PEG; number signifies the mean molecular weight of the PEG polymer). PEG400 was added to a concentration of 20% (v/v) to the yeast S100 extract while stirring at 18°C and incubated for 30 minutes. Precipitated proteins were removed by centrifugation at 30,000 rcf for 30 minutes at 4°C. The supernatant was then precipitated by raising the concentration of PEG400 to 30% (v/v) as described above. The precipitate of this step, which contains FAS, was recovered by centrifugation at 30,000 rcf for 30 minutes at 4°C and resuspended in purification buffer containing 2% (w/v) sucrose, 10 mM DTT and 0.01% (w/v) Lauryl Maltose Neopentyl Glycol (LMNG) in an orbital shaker at 18°C. The resuspended material was loaded on 10-45% (w/v) linear sucrose gradients in purification buffer containing 10 mM DTT, which were centrifuged at 100,000 rcf for 16 hours at 4°C. Gradients were harvested in 1 mL fractions. SDS-PAGE was utilized to identify fractions containing FAS. Selected fractions were pooled and precipitated by the addition of 40% (v/v) PEG400. After centrifugation (30,000 rcf, 30 minutes), the supernatant was removed and the precipitate was resuspended in purification buffer containing 2% (w/v) sucrose, 10 mM DTT and 0.01% (w/v) LMNG. The resuspended material was loaded on linear 10-45% (w/v) sucrose

gradients in purification buffer containing 10 mM DTT, and centrifuged at 79,000 rcf for 16 h at 4°C. Fractions containing FAS were identified by SDS-PAGE, pooled and cycled in the presence of 50 μM Malonyl CoA and 100 μM of NADPH for 30 min at 18°C ("cycled" FAS). For the FASx sample, cycling of FAS by addition of Malonyl CoA and NADPH was omitted ("uncycled" FAS). The protein was precipitated and concentrated by the addition of 40% (v/v) PEG400 and resuspended in purification buffer containing 2% (w/v) sucrose, 10 mM DTT and 0.01% (w/v) LMNG. Another round of linear 10-45% (w/v) sucrose gradients in purification buffer containing 10 mM DTT, centrifuged at 60,000 rcf for 16 hours at 4°C and subsequent re-precipitation of FAS fractions with 40% (v/v) PEG400 was required to yield a final purified protein preparation at ~15 mg/mL in purification buffer containing 10% sucrose (w/v), 10 mM DTT and 0.01% (w/v) LMNG. Protein concentrations were determined by Bradford assay (BioRad, Munich, Germany) using a BSA standard. The protein concentration was kept at ~15 mg/mL.

Purification of recombinant proteins

For the purification of γ-1xUnaG, γ-2xUnaG, γ-Tes, or Tes the frozen cell paste from overexpressing cells were resuspended in 5 mL resuspension buffer per gram of cells. The suspension was incubated (30 min, 4°C, mixing) after adding 2 U/mL DNAse (NEB) and 0.33 mg/mL lysozyme. Cells were lysed by passing two rounds through an Emulsiflex C3 (Avestin) at 15,000 PSI, the lysate was centrifuged (50,000 g, 30 min, 4°C) filtered through a cellulose-acetate syringe filter (Sartorius Stedim) and loaded on a 10 mL Ni-NTA column pre-equilibrated in 20 CV of resuspension buffer (0.05 M BisTris pH 6.5, 0.05 M potassium acetate, 0.01 M magnesium acetate, 0.01 M Imidazole). After binding of the protein of interest, the column was washed with 10 CV of washing buffer (0.05 M BisTris pH 6.5, 0.5 M potassium acetate, 0.01 M magnesium acetate, 10 mM Imidazole). For elution, 5 CV of elution buffer (0.05 M BisTris pH 6.5, 0.05 M potassium acetate, 0.01 M magnesium acetate, 0.5 M Imidazole) was applied and 1 mL fractions collected. The elution fractions were analyzed by SDS-PAGE and corresponding fractions pooled. The pooled protein solution was then digested by addition of TEV-protease in an enzyme-to-protein ration of 1:50. The digestion reaction was performed overnight (16 hours, 4°C, gently mixing) in a dialysis tube (6,000-8,000 MWCO) against 5 L of dialysis buffer (0.05 M BisTris pH 6.5, 0.05 M potassium acetate, 0.01 M magnesium acetate, 5% (w/v) sucrose). To remove the affinity tag, TEV protease, as well as undigested protein, the dialyzed protein solution was loaded on a 10 mL Ni-NTA column equilibrated with 10 CV dialysis buffer. The flow-through was collected and analyzed by SDS-PAGE. For concentration of the final protein, centrifugal filters of appropriate pore size were used, and the protein concentration was determined spectroscopically using the specific extinction coefficient as well as the molecular weight calculated from sequence. The final protein solutions were aliquoted, frozen in liquid nitrogen and stored at -80°C.

Cryo-EM sample preparation

For the FASx sample, "uncycled" FAS was diluted to 0.5mg/mL using cryo buffer (0.05 M BisTris pH 6.5, 0.05 M potassium acetate, 0.01 M magnesium acetate, 10 mM DTT). For the 1.9 Å FAS structure (FASmn), cycled FAS was diluted to 2 mg/mL using cryo buffer and incubated with 1 mM Malonyl CoA and 2 mM $NADP^+$ at 30°C for 30 min followed by transfer to 4°C. For the FASamn sample, cycled FAS was diluted to 2 mg/mL using cryo buffer and incubated with 20 μM Acetyl CoA, 1 mM Malonyl CoA and 2 mM $NADP^+$ at 30°C for 30 min followed by transfer to 4°C. For the FASam sample, cycled FAS was diluted to 2 mg/mL using cryo buffer and incubated with 1 mM Acetyl CoA and 1 mM Malonyl CoA at 30°C for 30 min followed by transfer to 4°C. The sample were kept at 4°C until grid preparation.

Cryo-EM grid preparation

UltrAuFoil R1.5/1.6 300-mesh grids (Quantifoil, Jena) were used for the FAS in the presence of Malonyl-CoA and $NADP^+$. The grids were pre-floated with custom-made continuous carbon foil covering ~25% of the grid area for alignment purposes. For the FASx and FASam samples, Quantifoil R3.5/1 (Cu), 200 Mesh grids were used, whereas for the FASamn sample, Quantifoil R2/2 (Cu), 200 Mesh grids were used. The grids were glow discharged for 30 seconds with a glow discharger built in-house under low vacuum shortly prior to sample application. For the FASmn and FASamn samples, 4 μL of the respective protein solution was applied to the glow-discharged grids, which were blotted for 6.5 seconds and plunge-frozen with a Vitrobot Mark IV (Thermo Fisher Scientific, Eindhoven) operated at 4°C and 100% humidity. For the FASx and FASam sample, the particles were adsorbed to a continuous carbon film attached to a Quantifoil (3.5/1) (Quantifoil, Jena, Germany) grid for 2 min at 4°C. The grid was then transferred to a Vitrobot Mark IV plunge-freezer where 4 μL of ddH_2O was applied to the grid followed by blotting and vitrification as described above.

Cryo-EM data collection and image processing

FAS structure in the presence of $NADP^+$ and Malonyl-CoA

All cryo-EM data were collected in nanoProbe mode on a Titan Krios electron microscope operating at 300 kV equipped with a monochromator (ThermoFisher Scientific, Eindhoven) and an aplanatic image corrector "B-Cor" (CEOS, Heidelberg). The monochromator was tuned to operate at 3 kV potential and excitation (0.8) to obtain an energy spread of the source of about 0.1-0.15 eV. The B-Cor was set-up to correct for off-axial aberrations, and beam-image shift induced coma and higher order electron optical aberrations and for linear distortions. For each cryo-EM dataset, the BCor was tuned with the signals from the amorphous carbon i) to correct the phase errors introduced by on-axis electron optical aberrations to less than 45 degrees at scattering angles $\geq$ 17 mrad, which is equivalent to $\leq$1.16 Å resolution, and ii) to reduce linear distortions to $\leq$0.2%. A total of 30659 movies with 40 fractions each were collected (Table S1). The exposure time was over 18.54 seconds with a dose of ~1.25 e/$Å^2$ per fraction in electron counting

mode using a Falcon III direct electron detector (ThermoFisher Scientific, Eindhoven) at a nominal magnification of 96000X (~0.615 Å/pixel) and 0.5 μm to 2.4 μm underfocus resulting in a total dose of ~50 e/Å^2. An adapted version of the software EPU (Thermo Fisher Scientific, Eindhoven) was used to acquire data by beam-image shift over up to 3 X 3 holes where five movies were acquired per hole. All image processing was performed using RELION 3.1,[38] if not indicated otherwise. Global motion correction and dose-weighting were performed using RELION's implementation of MotionCorr2[41] with a B-factor of 150. The power spectrum of aligned frames were used for CTF estimation by CTFFIND 4.1.13.[32] Particles were picked with reference to 2D templates using Gautomatch (from Dr. K. Zhang) and extracted with 4X binning (4.26 Å/pixel, 90 pixel box). Three rounds of reference-free 2D classifications were performed to remove bad particles. The remaining particles were re-centered and re-extracted in a 180 pixel box (2.13 Å/pixel) and subjected to 3D classification using C1 symmetry to distinguish intact particles from broken ones. The FAS structure (EMDB-4578) was low pass filtered to 45 Å and used as the 3D reference. The intact particles were then selected and re-extracted in a 560 pixel box (0.615 Å/pixel). 3D refinement while imposing D3 symmetry was then performed, resulting in a 2.45 Å structure (FSC 0.143 criterion). A round of CTF refinement was performed on the 3D refined particles to correct for per-micrograph defocus and per-micrograph astigmatism. Then, particle motion and the corresponding per-frame relative B factors were estimated by Bayesian polishing. The polished particles were subjected to a second round of 3D refinement which resulted in a 1.98 Å structure. Another round of CTF refinement was performed to correct for per-particle defocus and per-particle astigmatism. Afterwards, the particles were again subjected to Bayesian polishing where they were extracted with 920-pixel box (0.615 Å/pixel) followed by a third round of 3D refinement. Ewald sphere correction[42,43] was performed on the two resulting half-maps yielding a final reconstruction with a nominal resolution of 1.87 Å.

FAS asymmetric units in the FASx, FASamn and FASam samples

Data were acquired on a Titan Krios (ThermoFisher Scientific) operating at 300 kV using a Falcon 3 (linear mode) detector. Data collection and processing statistics are summarized in Table S1. Image processing of the acquired movies were performed in a similar manner as for described above until the 3D classification step. The selected intact particles were then used for another round of 3D classification (C1 symmetry).

In the FASx dataset, 162079 particles adopted a rotated conformation whereas 35927 particles were in the non-rotated conformation. The two sets of particles were processed separately. The selected particles were then used for 3D refinement (C1 symmetry). In particles with a rotated conformation, three ACP densities were found per dome adjacent to the AT domains. In the particles with a non-rotated conformation, nine ACP densities were found per dome; three each adjacent to the AT, KS and MPT domains. Since, each FAS dome can contain only 3 ACP domains, the particles with the non-rotated conformation were used for further rounds of 3D classification (C1 symmetry). However, all the 3D classes of FAS obtained contained at least 6 partial ACP densities per dome suggesting a random distribution of the ACP domains within the two domes. To sort for the different ACP bound states, a strategy involving symmetry expansion and signal subtraction was used in a similar manner as described before.[27] For this, the particle belonging to the non-rotated conformation were used for 3D refinement (D3 symmetry) followed by symmetry expansion using "relion_particle_symmetry_expand" function in RELION. A mask comprising of an αβ dimer as well as ACP domains at the AT, KS and MPT domains was used to *in silico* extract each asymmetric unit from each FAS molecule. The asymmetric unit were then 3D classified without alignment using a mask around the three possible positions of the ACP domain to sort for the different ACP's located at different active sites. Four distinct classes were observed where the ACP was located at either AT/KS/MPT domain or not visualized. The particles from each class were then 3D classified (without alignment) separately without any mask to sort for different conformational state of the αβ dimer. The particles with the rotated conformation were also processed in a similar manner as for the ones adopting the non-rotated conformation.

In the FASamn dataset, all particles were found to have a non-rotated conformation after 3D classification. However, each dome contained six ACP densities, three for ACP at the KR domain and three for ACP at the KS domain. Therefore, particle symmetry expansion and signal subtraction followed by 3D classification as described for the FASx dataset was performed.

In the FASam dataset, all particles were found to have a non-rotated conformation after 3D classification. However, each dome contained six ACP densities, three for ACP at the ER domain and three for ACP at the KS domain. Therefore, particle symmetry expansion and signal subtraction followed by 3D classification as described for the FASx dataset was performed. The distribution of the particles in different 3D classes for all the three datasets is summarised in Figure S2.

Cryo-EM Model building

The crystallographic Δγ-FAS model (PDB-6QL9) was used as the initial model for the 1.87Å FAS map. It was docked into the EM densities as a rigid body using UCSF Chimera.[39] An additional round of rigid body refinement was then performed in Refmac5.[37] The model then underwent several rounds of manual modelling in Coot[33] and refinement in Refmac5. Water molecules were built into the map through a combination of Coot and manual modelling and all waters with a Bfactor above 70Å^2 after refinement were not included.

The model obtained from the 1.87 Å FAS map was then used as the initial model for the FAS asymmetric units with ACP domains bound to enzymatic domains. The asymmetric unit comprising a single αβ dimer was docked into the EM densities as a rigid body using UCSF Chimera[39] and then the models underwent several rounds of manual modelling in Coot[33] and refinement in Refmac5.[37]

For model validation, Fourier Shell Correlation (FSC) between the refined model and the map was calculated (FSC_{sum}). The model was also refined using the first unfiltered half-map. This model was then compared to the first half map (FSC_{work}) as well as to the

second half-map (FSC_{free}) to check for signs of overfitting. In Table S1, the RMS deviation are from Refmac5 whereas the other values were calculated using the Phenix software package.[35] All figures were made using Pymol,[36] UCSF Chimera[39] and ChimeraX.[40]

Enzyme assays and semiquantitative analysis of CoA derivatives

For semiquantitative product analysis measurements of different FAS enzyme assays, 253.8 nM of freshly purified FAS was mixed with a 500X molar excess of γ-subunit or TesA-constructs, respectively. All reactions were incubated for 30 min at 25°C to ensure a binding of the added proteins to FAS and subjected to density gradient centrifugation. To the density gradient peak fractions, final co-substrate concentrations of 100 μM (acetyl-CoA), 60 μM (malonyl-CoA) and 320 μM (NADPH) were added and enzymatic reactions initiated. After an incubation for 30 min at 30°C, the reactions were quenched by shock-freezing in liquid nitrogen. In the subsequent treatment with TesA 6 μM was added before shock-freezing. CoA thioesters were analyzed according to a method adapted from Wolf et al.[44] Methanol was replaced by acetonitrile to facilitate the analysis of acyl-CoAs up to C_{20}-acyl-CoA, and the gradient was adapted to allow the separation of derivatives of higher polarity (e.g. malonyl-CoA and free CoA). The metabolites were analyzed by HPLC-MS using an Agilent 6545 QTOF system equipped with an ESI source coupled to a 1290 series HPLC system. One μL of the enzyme assay without any further treatment was directly injected onto a Gemini C18 column (3 μm, 110 Å, 150 X 2 mm). The solvent used were 50 mM ammonium formate, pH 8.1 (A) and acetonitrile (B) at 35°C with the following gradient: 95% A for 1 min, gradient to 30% B in 18 min, gradient to 95% B in 17 min and gradient to 100% B in 4 min. The QTOF was run at following settings: positive mode, gas temperature 200°C, Sheath gas temperature 325°C, Fragmentor 180 V, Skimmer 45 V, Capillary voltage 4500 V. Data were evaluated using the MassHunter Qualitative Navigator software (version B08.00, Agilent Technologies, Santa Clara, CA, USA) by extracting ion chromatograms for the $[M+H]^+$ and the $[M+2H]^{++}$ m/z of the respective CoA thioesters. The retention time was confirmed by the use of authentic standards.

Sequence conservation analysis

We analysed the sequence conservation of ACP binding sites at different catalytic sites between *S. cerevisiae* and *Y. lipolytica*. For this, we first generated a multiple sequence alignment of the FAS genes from these two species using Clustal Omega[31] followed by mapping the sequence conservation onto the different ACP bound states of *S. cerevisiae* FAS using ChimeraX.[40]

QUANTIFICATION AND STATISTICAL ANALYSIS

Calculating ACP distribution per asymmetric unit

Based on the results of the 3D classification after signal subtraction a label was assigned to every asymmetric unit. Asymmetric units were then traced back to their respective FAS molecules in the RELION particle star file. The information gathered was then compiled into a table and analyzed in a similar manner as described by Roh et al.[27] In brief, we used computational analysis to capture correlation among asymmetric units by using normalized mutual information, which measures the conformational correlation between a pair of subunits. To compare the NMI distribution of the data with a random distribution, we generated 100 replicate shuffled datasets based on the original data. In the replicated data, each particle in the original data was rotated at random. The calculation of ACP distribution per asymmetric unit/FAS molecule was then performed using PANDAS.[45]

Semiquantitative analysis of CoA derivates

All enzymatic reactions were performed in triplicate. The total CoA content was expressed as 100% for each individual reaction. From these values averages and error bars calculated. The relative abundance of individual acyl-CoAs is represented as a fraction of the total CoA content.

CellPress
OPEN ACCESS

Supplemental figures

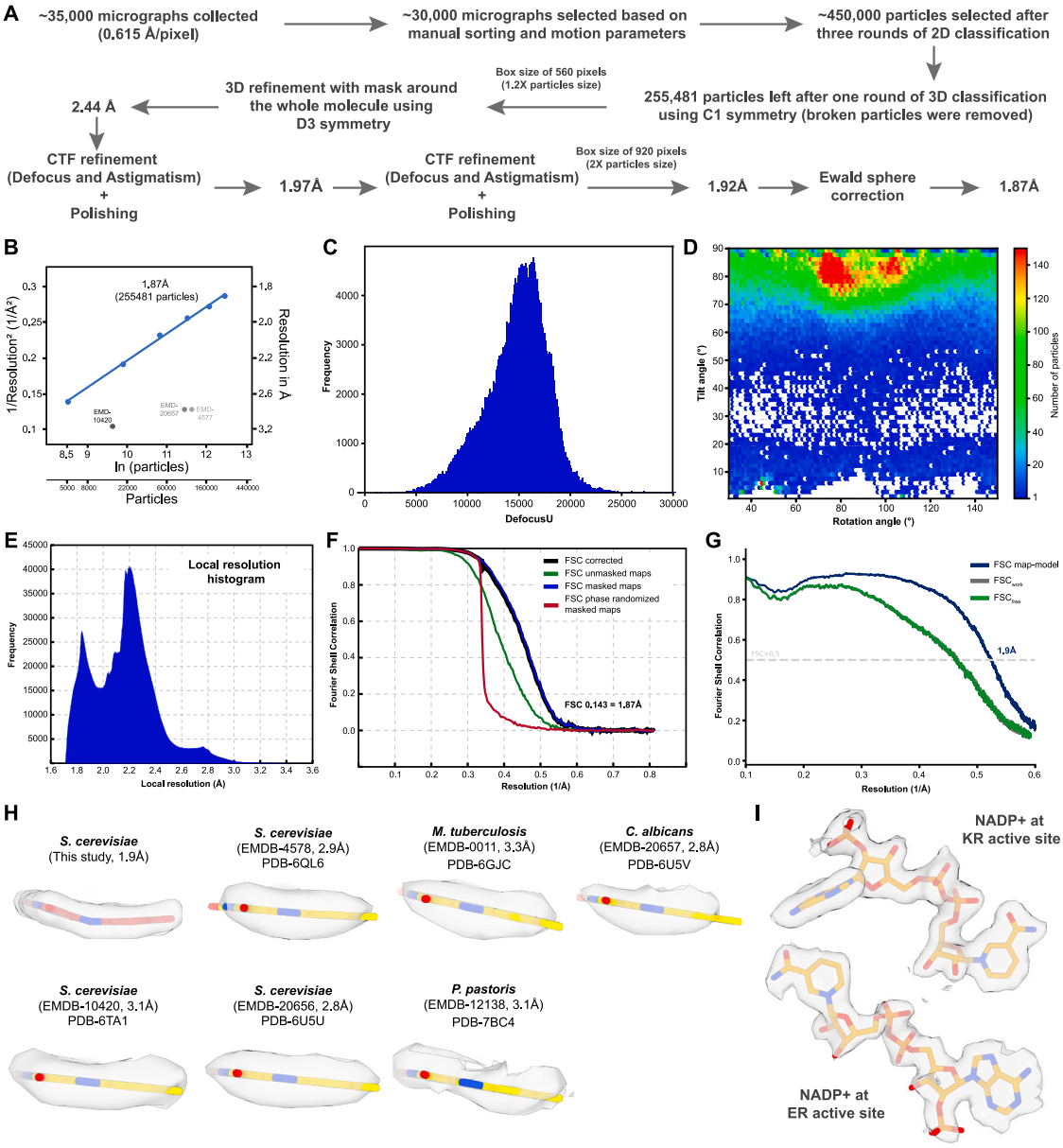

Figure S1. Cryo-EM data processing for the 1.9Å FAS structure, related to Figure 1

(A) The image-processing scheme is depicted.

(B) B-factor plot for Δγ-FAS in the presence of malonyl-CoA and $NADP^+$ imaged using the Krios Mono/BCOR electron microscope. A B-factor of $53Å^2$ was obtained using 255,481 particles, which yielded a 1.9Å structure (as per the FSC 0.143 criterion).

(C) Histogram denoting the distribution of micrograph defocus values.

(D) Euler angle distribution plot.

(E) Histogram for the local resolution distribution.

(F) Fourier shell correlation (FSC) between the two half-maps obtained after the final 3D refinement.

(G) FSC between the final map and model (FSCsum; blue), FSCwork (gray), and FSCfree (green) curves for validation of the model refined against the cryo-EM map.

(H) Comparison of ER FMN density in various structures of type I FAS.[11,15–18] Former structures do not unequivocally resolve the isoalloxazine kink.

(I) Density corresponding to $NADP^+$ at KR and ER active sites.

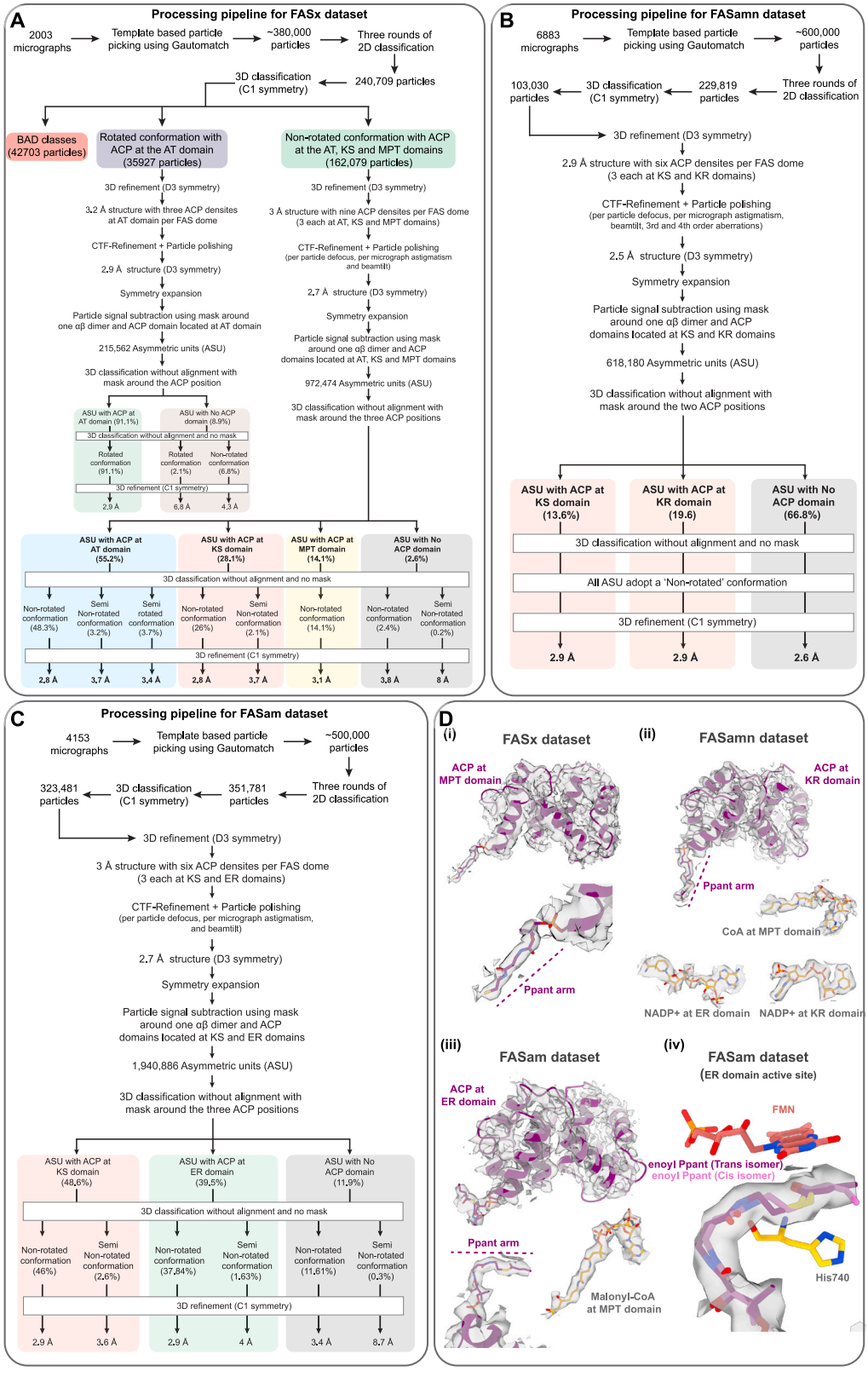

(legend on next page)

Figure S2. Cryo-EM data processing schemes for ACP-bound datasets, related to Figures 2, 3, 4, and 5

(A–C) Image-processing schemes for the FASx (A), FASamn (B), and FASam (C) datasets are depicted.

(D) Density of ACP and bound ligands at different catalytic domains is depicted:

(i) Density corresponding to the MPT-domain-bound ACP and its Ppant arm from the FASx dataset.

(ii) Density corresponding to the KR-domain-bound ACP and its Ppant arm as well as bound co-substrates from the FASamn dataset.

(iii) Density corresponding to the ER-domain-bound ACP and its Ppant-arm as well as MPT-bound CoA molecule from the FASam dataset.

(iv) Overlay of the trans and *cis* isomers of the Ppant-bound enoyl intermediate. The ER catalytic cleft can structurally accommodate either isomer.

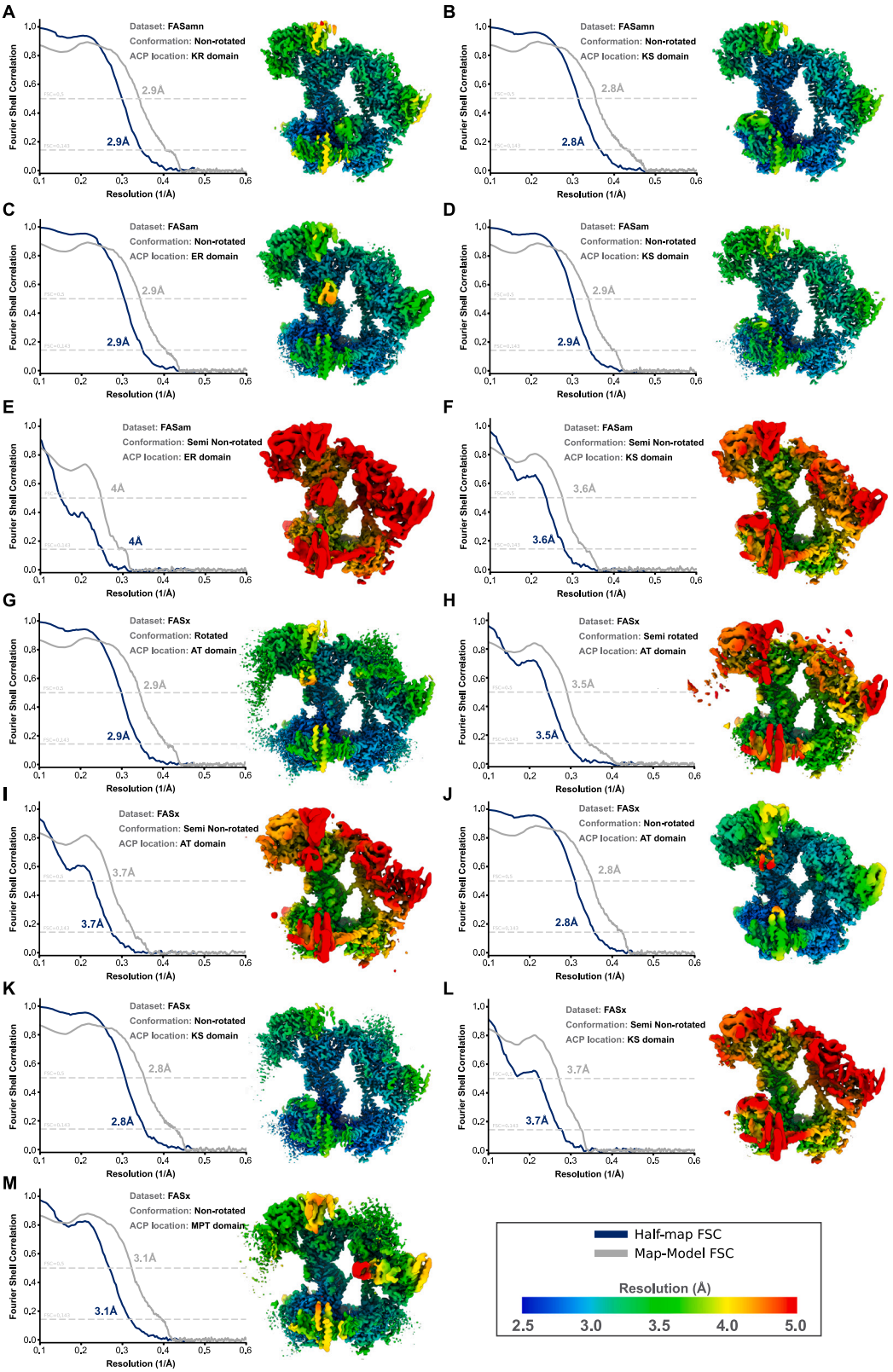

(legend on next page)

Figure S3. Fourier shell correlation and local resolution distribution of the ACP-bound structures of the FAS asymmetric units (ASUs), related to Figures 2, 3, 4, and 5

(A and B) ASUs from the FASamn dataset with (A) non-rotated conformation and ACP bound at the KR domain and (B) non-rotated conformation and ACP bound at the KS domain.

(C–F) ASUs from the FASam dataset with (C) non-rotated conformation and ACP bound at the ER domain, (D) non-rotated conformation and ACP bound at the KS domain, (E) semi-non-rotated conformation and ACP bound at the ER domain and (F) semi-non-rotated conformation and ACP bound at the KS domain.

(G–M) ASUs from FASx dataset with (G) rotated conformation and ACP bound at the AT domain, (H) semi-rotated conformation and ACP bound at the AT domain, (I) semi-non-rotated conformation and ACP bound at the AT domain, (J) non-rotated conformation and ACP bound at the AT domain, (K) non-rotated conformation and ACP bound at the KS domain, (L) semi-non-rotated conformation and ACP bound at the KS domain, and (M) non-rotated conformation and ACP bound at the MPT domain.

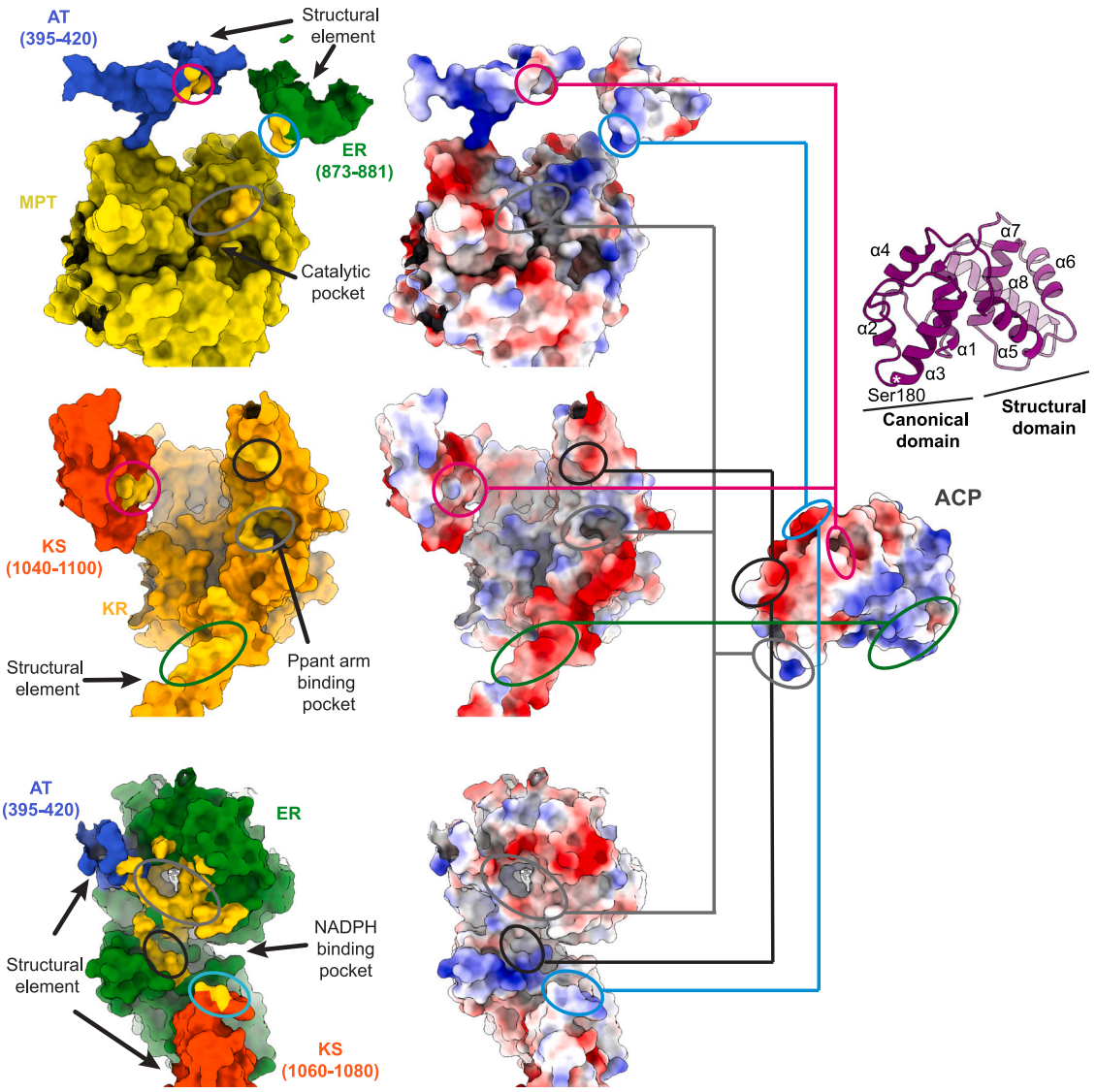

Figure S4. Surface and electrostatic representation of ACP interactions with MPT, KR, and ER domains, related to Figure 3

The ACP-interacting regions on the surface of the different domains are highlighted in gold (left). The electrostatic surface representation of the MPT, KR, and ER domains and proximal structural elements (center) and the ACP domain (right) illustrates that ACP interactions at the different sites involve charge complementarity.

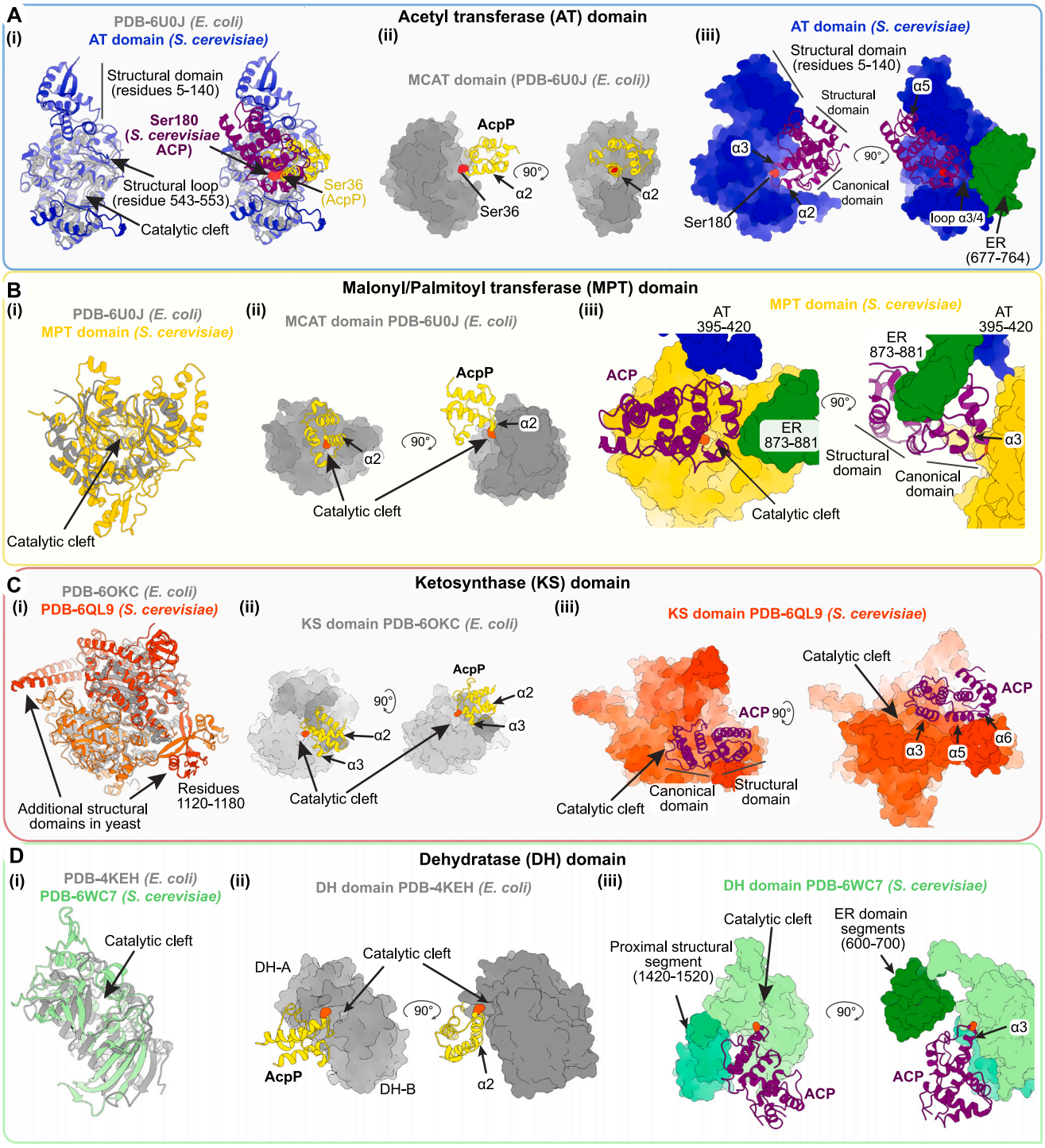

Figure S5. ACP binding and domain comparison between bacterial type II and *S. cerevisiae* type I FAS systems, related to Figures 3 and 4

The ACP-bound malonyl coenzyme A-acyl carrier protein transacylase (MCAT) enzyme (*E. coli*, PDB: 6U0J),[23] which is homologous to *S. cerevisiae* type I FAS (yFAS) AT and MPT domains, and the ACP-bound structures of *E. coli* dehydratase (FabA, PDB: 4KEH[6]), ketosynthase (FabB, PDB: 6OKC)[24] were compared with their fungal counterparts.

(A) Acetyl transferase domain.

(i, left) Overlay of *E. coli* MCAT enzyme (gray) with the yFAS AT domain (blue). The yFAS AT domain has structural segments in addition to the conserved fold of the catalytic domain. (i, right) Overlay of ACP domain bound to the *E. coli* MCAT enzyme (AcpP; yellow) and yFAS AT domain (ACP; purple). The Ppant-serine is highlighted in orange.

(legend continued on next page)

(ii and iii) Comparison of ACP bound to the *E. coli* MCAT enzyme (ii) with ACP bound to yFAS AT domain (iii). Even though the Ppant-serine (Ser36 for *E. coli* AcpS and Ser180 of yFAS ACP) is located at the entrance of the catalytic cleft in both ACP-bound structures, the interaction interfaces between ACP, and catalytic domains differ. The yFAS ACP cannot bind in the AcpP-MCAT pose due to clashes with the AT structural loop (543–553) and the adjacent ER domain segments (ii and iii). Instead, yFAS ACP interacts with the AT catalytic domain via α helices 2 and 3, with ER domain segments (green) using the loop connecting α helices 3 and 4, and via helix 5 to the AT structural domain (iii). The yFAS AT-ACP interaction interface with a buried surface area of $\sim$1,033 Å^2 is almost twice as large as the MCAT-AcpP interaction, which buries a surface area of 459 Å^2.

(B) Malonyl/palmitoyl transferase.

(i) Overlay of *E. coli* MCAT enzyme (gray) with the yFAS MPT domain (golden). The yFAS MPT domain also has structural segments in addition to the conserved fold of the catalytic domain.

(ii and iii) Comparison of AcpP (yellow) bound to *E. coli* MCAT enzyme (ii) with ACP (purple) bound to yFAS MPT domain (iii). The position of the Ppant-serine is indicated in orange. AcpP contacts MCAT via its α helix 2 and the loop connecting α helices 2 and 3. In comparison, yFAS ACP contacts the MPT domain via its α helix 3 and nearby structural segments of ER (green) and AT (blue) domains through α helices 4 and 5, respectively. These additional interactions stabilize the ACP.

(C) Ketosynthase.

(i) Overlay of *E. coli* KS enzyme (gray) with the yFAS KS domain (orange). Similar to bacterial KS, the yFAS KS domain dimerizes; however, in addition to the conserved catalytic domain, structural segments exist in yFAS KS.

(ii and iii) Comparison of ACP bound to *E. coli* KS enzyme (AcpP; yellow) (ii) with ACP bound to yFAS KS domain (ACP; purple) (iii). The position of the Ppant-serine is indicated in orange. AcpP contacts the KS via α helices 2 and 3, whereas in yFAS, ACP α helix 3 of the canonical domain contacts the KS domain in a manner distinct to the AcpP-KS interaction. The yFAS ACP-KS interaction is additionally stabilized by ACP α helices 5 and 6 of the structural domain interacting with KS structural segments (1,120–1,180).

(D) Dehydratase.

(i) Overlay of *E. coli* dehydratase enzyme (gray) with the yFAS dehydratase domain[12] (light green). The *E. coli* dehydratase (FabA) forms a dimer, whereas in yFAS it has a pseudo-dimeric organization.

(ii and iii) Comparison of ACP bound to *E. coli* DH enzyme (AcpP; yellow) (ii), with ACP bound to yFAS DH domain (ACP; purple) (iii). The position of the Ppant-serine is indicated in orange. *E. coli* AcpP interacts with FabA mainly via its α helix 2. The interaction of ACP with yFAS DH is primarily mediated by α helix 3, and the poses of the bacterial and yFAS ACPs differ with respect to the respective DH. In the case of yFAS ACP, proximal DH structural elements (1,420–1,520) and the ER domain (green) prevent adopting an AcpP-like binding pose (iii).

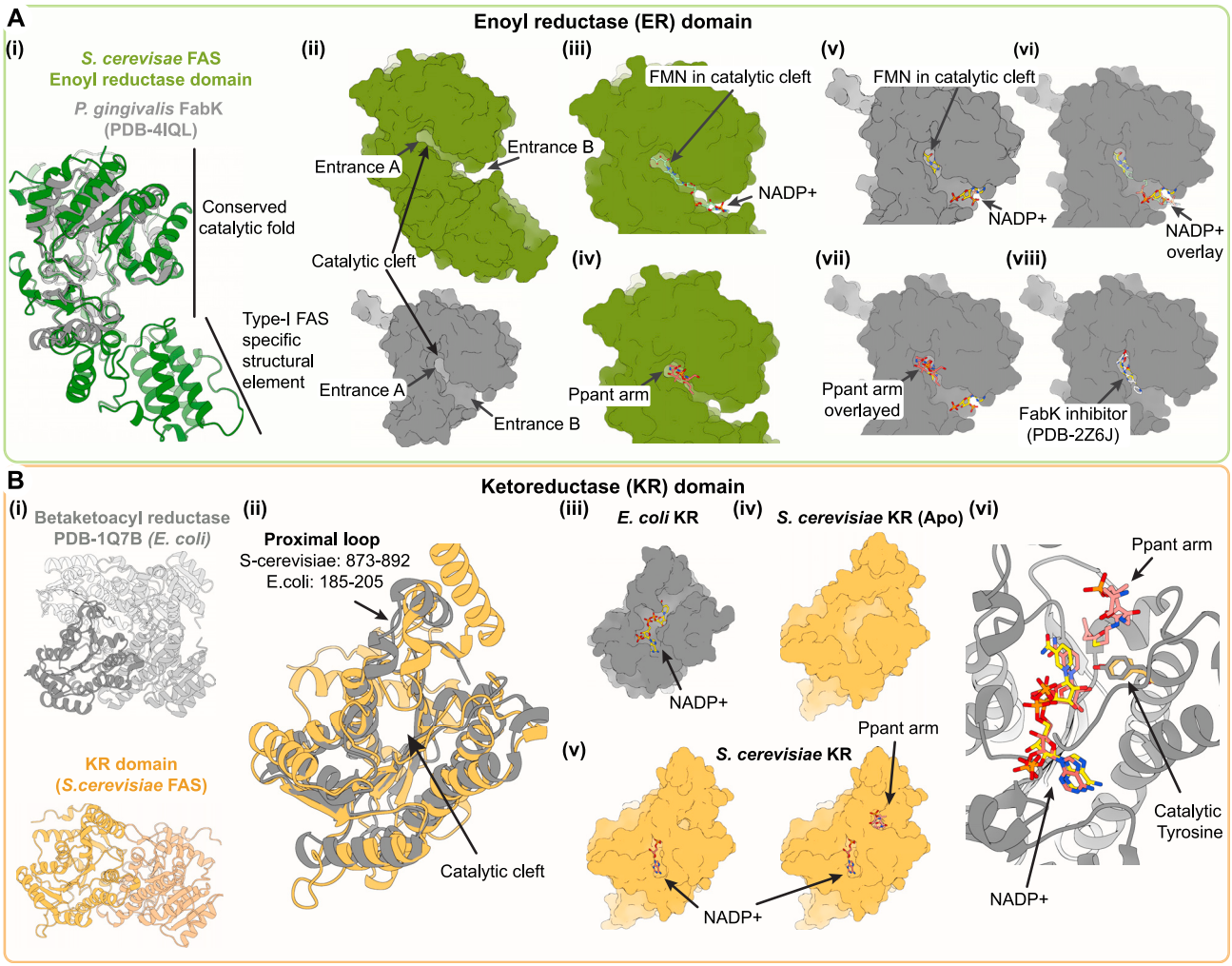

Figure S6. Comparison of structural features of bacterial type II enoyl- and ketoreductases to fungal type I counterparts, related to Figures 3 and 4

Since there are presently no deposited structures of ACP bound to the fungal-like ER (FabK) and KR domains of the type II FAS system, only broad comparisons can be performed with regards to complementarity of ACP recognition between type I and type II systems in these cases.

(A) Enoyl reductase.

(i) Overlay of *P. gingivalis* FabK enzyme (PDB: 4IQL,[25] gray) with the yFAS ER domain (green).

(ii) Surface representation of FabK (gray) and yFAS ER domain (green). Both yFAS ER domain and the bacterial FabK exhibit an active site cleft with two entrances and a bound FMN cofactor, with additional segments in yFAS ER playing a structural role.

(iii and iv) NADPH/$NADP^+$ enters through entrance B (iii), whereas the ACP-bound Ppant group gains access through entrance A (iv).

(v and vi) In the FabK-$NADP^+$ structure, only the ADP moiety was resolved (v) and the overlay of the $NADP^+$-bound yFAS ER with FabK (vi) suggests that the NADPH/$NADP^+$ would be bound in a similar manner by FabK.

(vii and viii) Overlaying Ppant-group-bound scFAS ER with FabK (vii) suggests that entrance A in FabK would be able to similarly accommodate a Ppant group into the active site. Notably, a FabK inhibitor binds in the Ppant binding pocket and acts as a competitive inhibitor to NADPH/$NADP^+$ (viii).

(B) Ketoreductase.

(i) Bacterial KR (FabG, PDB: 1Q7B,[26] gray) is a tetramer, whereas the yFAS KR (orange) dimerizes.

(ii–iv) The catalytic fold of the KR is well conserved between the two FAS system types. The active site cleft $NADP^+$-bound *E. coli* KR (iii) is much more open than the $NADP^+$-bound yFAS KR (v, left), where the proximal loop clamps onto the bound co-substrate and creates a pocket for Ppant-arm entry (v, right).

(vi) Overlay of the $NADP^+$-bound FabG with ACP-bound yFAS KR domain. As both bound $NADP^+$ and the catalytic tyrosine residue adopt similar positions in both type II and type I KR, one can infer that the Ppant arm in bacterial KR would be similarly positioned, as observed here for yFAS KR.

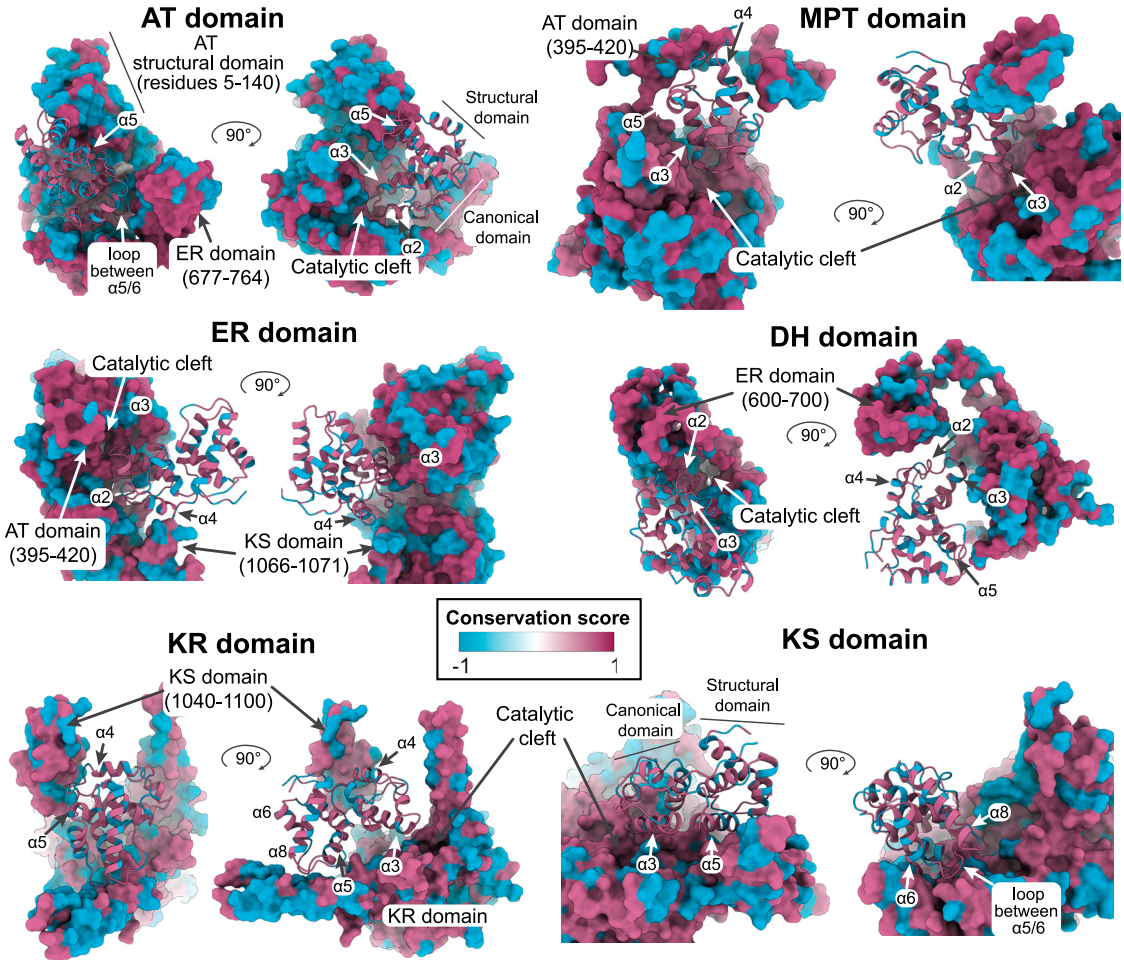

Figure S7. Sequence conservation between the *S. cerevisiae* FAS and the oleaginous, biotechnologically important yeast *Y. lipolytica* FAS, related to Figures 3 and 7

The sequence conservation is mapped onto the models where the residues are colored based on their conservation score (−1: diverged, colored in teal, to 1: conserved, colored in magenta). The different domains and neighboring structural elements are depicted in a surface representation, whereas the ACP domain is drawn as a cartoon. The conservation analysis suggests that most ACP sequences involved in active site contacts or contacting adjacent structural elements near active sites are conserved. The same holds true for FAS segments in direct contact with the ACP. Further, interacting interfaces that have a larger buried interface are better conserved, suggesting that those are largely responsible for the recognition process. This entails α helices 2, 3, and 5, the loops between α5/6 and α7/8 of the ACP, and the regions of the different FAS domains that interact with these segments. In comparison, regions where only one or two amino acids interact with each other are more poorly conserved; for example, this applies for the loop between α4/5.